

- 1 Title: On time delay estimation and sampling error in resting-state fMRI
- 2 Authors: Ryan V. Raut<sup>1,\*</sup>, Anish Mitra<sup>1</sup>, Abraham Z. Snyder<sup>1,2</sup>, & Marcus E. Raichle<sup>1,2</sup>
- 3 Affiliations: Departments of <sup>1</sup>Radiology and <sup>2</sup>Neurology, Washington University, St. Louis, MO
- 4 63110
- 5 \*Address correspondence to: [raut@wustl.edu](mailto:raut@wustl.edu)

## 6 **ABSTRACT**

7 Accumulating evidence indicates that resting-state functional magnetic resonance imaging  
8 (rsfMRI) signals correspond to propagating electrophysiological infra-slow activity ( $<0.1$  Hz).  
9 Thus, pairwise correlations (zero-lag functional connectivity (FC)) and temporal delays among  
10 regional rsfMRI signals provide useful, complementary descriptions of spatiotemporal structure  
11 in infra-slow activity. However, the slow nature of fMRI signals implies that practical scan  
12 durations cannot provide sufficient independent temporal samples to stabilize either of these  
13 measures. Here, we examine factors affecting sampling variability in both time delay estimation  
14 (TDE) and FC. Although both TDE and FC accuracy are highly sensitive to data quantity, we  
15 use surrogate fMRI time series to study how the former is additionally related to the magnitude  
16 of a given pairwise correlation and, to a lesser extent, the temporal sampling rate. These  
17 contingencies are further explored in real data comprising 30-minute rsfMRI scans, where  
18 sampling error (i.e., limited accuracy owing to insufficient data quantity) emerges as a significant  
19 but underappreciated challenge to FC and, even more so, to TDE. Exclusion of high-motion  
20 epochs exacerbates sampling error; thus, both sides of the bias-variance (or data quality-  
21 quantity) tradeoff associated with data exclusion should be considered when analyzing rsfMRI  
22 data. Finally, we present strategies for TDE in motion-corrupted data, for characterizing  
23 sampling error in TDE and FC, and for mitigating the influence of sampling error on lag-based  
24 analyses.

25 **Keywords:** time delay estimation, functional connectivity, lag, sampling error, head motion,  
26 reliability

## 27 1. INTRODUCTION

28           Since the seminal observations of Biswal and colleagues (Biswal *et al.*, 1995), interest in  
29 resting-state functional magnetic resonance imaging (rsfMRI) for the study of spontaneous brain  
30 activity has increased exponentially (Snyder and Raichle, 2012). Studying the zero-lag temporal  
31 correlation structure of spontaneous fluctuations in the blood oxygen level-dependent (BOLD)  
32 signal (i.e., “functional connectivity (FC)” analysis) provides an efficient means for mapping the  
33 large-scale spatial organization of brain function (Fox *et al.*, 2005; Damoiseaux *et al.*, 2006; Fox  
34 and Raichle, 2007; Power *et al.*, 2011; Yeo *et al.*, 2011). Although FC is the standard mode of  
35 rsfMRI analysis, spontaneous BOLD fluctuations additionally exhibit spatiotemporal dynamics  
36 not captured by zero-lag FC (i.e., processes whose measurement is contingent upon the  
37 temporal ordering of BOLD time points) (Liégeois *et al.*, 2017). In particular, rsfMRI signals  
38 reflect infra-slow (<0.1 Hz) electrophysiological activity (Hiltunen *et al.*, 2014; Palva and Palva,  
39 2012; Pan *et al.*, 2013), which exhibits stereotyped propagation patterns across the brain; this  
40 widespread propagation leads to reliable interregional time delays on the order of one second  
41 between BOLD signals (MatsuiMurakami and Ohki, 2016; Mitra *et al.*, 2018). The resultant  
42 temporal latency structure comprises multiple reproducible propagation sequences (Mitra *et al.*,  
43 2015a), is dramatically rearranged across arousal states (Mitra *et al.*, 2015b; Mitra *et al.*, 2016;  
44 Mitra *et al.*, 2018), and is sensitive to behavior (Mitra *et al.*, 2014) and pathology (Mitra *et al.*,  
45 2017) even in the absence of significant changes in FC. Thus, time delay estimation (TDE)  
46 provides a useful complement to zero-lag FC for characterizing spatiotemporal structure in  
47 rsfMRI.

48           Importantly, the predominance of very low frequencies (<0.1 Hz) in infra-slow activity  
49 and BOLD signals means that practical scan durations do not provide sufficient independent  
50 temporal samples to stabilize second-order statistical measures (Laumann *et al.*, 2015). These  
51 include cross-correlation among pairs of regional BOLD signals, from which both FC and time

52 delays can be derived (Fig. 1). There is growing appreciation for the consequences of such  
53 sampling variability on FC (Hlinka and Hadrava, 2015; Laumann *et al.*, 2015; Laumann *et al.*,  
54 2016; Hindriks *et al.*, 2016), although the effects of rsfMRI artifacts such as those arising from  
55 head motion have received more attention. Crucially, procedures such as temporal censoring  
56 (i.e., the exclusion of high-motion time points) are effective for mitigating artifact (Power *et al.*,  
57 2012) but at the cost of increased sampling error. Thus, it is important to consider both sides of  
58 the tradeoff between data quality and quantity, or between *bias* associated with specific artifacts  
59 and *variance* arising from reduced data quantity. Although the “correct” balance depends on the  
60 question of interest, in general, the latter becomes increasingly problematic the less stable a  
61 statistical measure is. Hence, sampling variability is a significant concern for correlations, and  
62 even more so for lag-based measures (Smith *et al.*, 2011). Further, temporal censoring  
63 complicates TDE, which generally requires contiguous data.

64         The primary goals of this work are to examine factors impacting TDE (and FC) sampling  
65 variability in fMRI, to address the integration of motion censoring with TDE, and to examine  
66 bias-variance tradeoffs in both TDE and FC. We begin with analyses of surrogate fMRI time  
67 series pairs with modeled time delays; these allow us to quantify, as a function of multiple  
68 factors, TDE and FC error with respect to “true” delays and correlations, respectively. Next, we  
69 use insights from these simulations to demonstrate how the effects of sampling variability in  
70 both TDE and FC can be easily observed in real data. Finally, we conclude with strategies to  
71 reduce the influence of sampling error on inferences drawn from TDE. Importantly, although  
72 interregional TDE is perhaps the most straightforward approach for quantifying BOLD  
73 propagation (Fig. 1), results are pertinent to the variety of approaches that have been used to  
74 detect or exploit temporal offsets among fMRI signals (Goebel *et al.*, 2003; SunMiller and  
75 D'Esposito, 2005; GargCecchi and Rao, 2011; Majeed *et al.*, 2011; Friston *et al.*, 2014; Mitra *et*

76 *al.*, 2014; Amemiya *et al.*, 2016; Gilson *et al.*, 2016; Raatikainen *et al.*, 2017) (see Friston *et al.*  
77 (FristonMoran and Seth, 2013; Friston *et al.*, 2014) for taxonomy of these approaches).

## 78 2. TIME DELAY ESTIMATION

### 79 2.1. Theory

80 The Pearson correlation coefficient,  $r$ , for zero-lag correlation (i.e., FC) between  
81 continuous signals,  $x_1(t)$  and  $x_2(t)$ , is given by:

$$82 \quad r_{x_1x_2} = \frac{1}{\sigma_{x_1}\sigma_{x_2}} \frac{1}{T} \int x_1(t) \cdot x_2(t) dt, \quad (1)$$

83 where  $\sigma_{x_1}$  and  $\sigma_{x_2}$  are the temporal standard deviations of the zero-mean signals  $x_1$  and  $x_2$  and  
84  $T$  is the interval of integration. By generalizing this equation to accommodate temporal delays,  $\tau$ ,  
85 between the signals, correlation (or covariance, for simplicity, where  $r_{x_1x_2}$  is not normalized by  
86 the signal standard deviations) can be computed as a function of delay in seconds. Thus,

$$87 \quad c_{x_1x_2}(\tau) = \frac{1}{T} \int x_1(t + \tau) \cdot x_2(t) dt \quad (2)$$

88 defines the cross-covariance function (CCF). The lag between  $x_1$  and  $x_2$ ,  $\tau_{1,2}$ , is then determined  
89 to be the value of  $\tau$  at which  $c_{x_1x_2}(\tau)$  exhibits an extremum. Thus,

$$90 \quad \tau_{1,2} = \arg \max_{\tau} (|c_{x_1x_2}(\tau)|). \quad (4)$$

91 While the CCF of periodic time series is likely to feature multiple extrema, BOLD signals are  
92 aperiodic (He *et al.*, 2010; ZarahnAguirre and D'Esposito, 1997) and almost always produces a  
93 single, well-defined cross-covariance extremum for a given pair of time series, typically in the  
94 range of  $\pm 1$  s.

### 95 2.2. Implementation

96 In practice, we first construct the CCF in the time domain at discrete multiples of the TR  
 97 (i.e., at the sampling interval). A single CCF for each session is obtained by summing  
 98 unnormalized cross-covariance over blocks ( $b$ ) of contiguous frames, and subsequently  
 99 normalizing based on the entire time series. (Variations of this approach are discussed in the  
 100 next section). Thus,

$$101 \quad c_{x_1 x_2}(\Delta) = \sum_{t=1}^{N_b} x_{1b}(t + \Delta) \cdot x_{2b}(t), \quad (5)$$

$$102 \quad c_{x_1 x_2}(\Delta) = \frac{1}{N_{\Delta=0}} \sum_{b=1}^B c_{x_1 x_2}, \quad (6)$$

103 where  $\Delta$  is the temporal shift in units of TRs,  $t$  indexes frames,  $N_b$  is the total number of frames  
 104 within the block,  $N_{\Delta=0}$  is the total number of frames contributing to the zero-lag CCF estimate,  
 105 and  $B$  is the total number of blocks. Because BOLD signals are best understood as stationary  
 106 random processes (Liégeois *et al.*, 2017), we set time series to zero-mean prior to Equation (5)  
 107 by subtracting the mean computed over the maximum number of realizations (i.e., all non-  
 108 censored frames from the time series), rather than de-meaning each block separately, which  
 109 would also increase the bias associated with CCF estimation (Marriott and Pope, 1954; Kendall,  
 110 1954).

111 We subsequently use three-point parabolic interpolation among the empirical peak of  
 112  $c_{x_1 x_2}(c_{peak})$  and the values immediately preceding ( $c_{peak-1}$ ) and succeeding ( $c_{peak+1}$ ) it in order  
 113 to approximate the extremum and its associated abscissa,  $\hat{t}_{1,2}$ , at a temporal resolution finer  
 114 than the sampling rate (Fig. 1A-B) (Mitra *et al.*, 2014):

$$115 \quad \hat{t} = \text{TR} \frac{c_{peak-1} - c_{peak+1}}{2(c_{peak-1} - 2c_{peak} + c_{peak+1})}. \quad (7)$$

116 We currently discount delays longer than four seconds ( $\hat{t}_{max} = 4$  s) as, in our experience,  
 117 such results appear to reflect sampling error or artifact. Because a given time delay will typically

118 result in a peak in the empirical CCF at the nearest multiple of the TR, a true time delay at the  
 119 maximum allowable ( $\tau = \hat{\tau}_{max}$ ) can be resolved by allowing at least that number of time shifts,  
 120 plus an additional time shift for parabolic interpolation ( $\Delta_{max} = \text{round}(\hat{\tau}_{max}/\text{TR}) + 1$ ), where  
 121  $\text{round}()$  evaluates to the nearest integer. In the present case ( $\text{TR} = 2.2$  s), three time shifts  
 122 ( $\Delta_{max} = 3$ ) were needed in each direction to estimate  $\tau = \hat{\tau}_{max}$ . Hence,  $c_{x_1x_2}(\Delta)$  was computed  
 123 over  $\Delta \in [-3, 3]$ .

124 The above approach can be generalized to a set of  $n$  time series  $[x_1(t), x_2(t), \dots, x_n(t)]$ .  
 125 Thus,  $C_{x_ix_j}(\Delta)$  will be an  $n \times n \times \Delta$  cross-covariance matrix from which  $\hat{\tau}_{x_ix_j}$  can be obtained for  
 126 every pair of time series,  $x_ix_j$  ( $i, j \in 1, 2, \dots, n$ ), yielding an  $n \times n$  time delay matrix:

$$127 \quad TD = \begin{bmatrix} \hat{\tau}_{1,1} & \cdots & \hat{\tau}_{1,n} \\ \vdots & \ddots & \vdots \\ -\hat{\tau}_{n,1} & \cdots & \hat{\tau}_{n,n} \end{bmatrix}. \quad (8)$$

128 The diagonal entries of  $TD$  are 0 by definition, given that a time series is perfectly correlated  
 129 with itself at zero-lag. Moreover,  $TD$  is anti-symmetric ( $\hat{\tau}_{i,j} = -\hat{\tau}_{j,i}$ ): if the time series  $x_i$  is  
 130 determined to precede  $x_j$  by a certain magnitude, then  $x_j$  can equivalently be said to succeed  $x_i$   
 131 by the same magnitude, yielding the opposite sign.

132 Here we compute  $\hat{\tau}_{i,j}$  as the temporal delay of  $x_j$  relative to  $x_i$ , such that a negative  
 133 value implies that  $x_j$  precedes  $x_i$ . Thus, in accord with Nikolic et al. (SchneiderHavenith and  
 134 Nikolić, 2006; Nikolić, 2007), a column-wise mean will yield a one-dimensional projection of  $TD$ ,  
 135 which we refer to as a “lag projection” ( $TD_p$ ), reflecting the mean latency of each region of  
 136 interest (ROI),  $n$ , with respect to all other ROIs. Hence,

$$137 \quad TD_p = \frac{1}{n} \left[ \sum_{j=1}^n \hat{\tau}_{1,j} \dots \sum_{j=1}^n \hat{\tau}_{n,j} \right]. \quad (9)$$

138 Further, for a given “seed” region comprising one or multiple ROIs, the entire rows of  $TD$   
139 corresponding to these ROIs can be averaged to give a seed-based lag map – a one-  
140 dimensional map of each voxel’s temporal delay with respect to the seed. The majority of real  
141 data presented here utilize a widely used set of 264 ROIs (Power *et al.*, 2011) for simplicity.  
142 Exceptions are Figures 1E, 5, and 10, which utilize 6 mm cubic gray matter voxels (Mitra *et al.*,  
143 2014) to provide uniform spatial coverage.

### 144 *2.3. TDE and motion censoring*

145 Unlike surrogate data, real fMRI data are contaminated by artifact generated by head  
146 motion, cardio-pulmonary pulsations and fluctuating arterial  $pCO_2$ , which poses challenges to  
147 accurately estimating time delays of interest. Rather than individually examining each of these  
148 artifact sources, we reason that existing denoising strategies (PowerSchlaggar and Petersen,  
149 2015; Liu, 2016; Caballero-Gaudes and Reynolds, 2017; Satterthwaite *et al.*, 2017) should  
150 improve TDE. However, one such technique, motion censoring (Power *et al.*, 2012), is worth  
151 revisiting in detail in the context of TDE.

152 Removal of high-motion time points (censoring or scrubbing) from rsfMRI data reduces  
153 motion artifact (Power *et al.*, 2012) but integration of censoring into TDE is not straightforward.  
154 Zero-lag correlation is invariant to re-ordering of data points within a time series, provided that  
155 the new ordering is common to both time series (Liégeois *et al.*, 2017). This means that, within  
156 each time series, time points on either side of flagged high-motion frames can be directly  
157 concatenated. However, when computing pairwise correlation or covariance as a function of  
158 time delay (i.e.,  $c_{i,j}(\Delta)$  where  $\Delta \neq 0$ ), the flagged frames of the shifted time series will be  
159 misaligned with those of the first time series (Fig. 2a). In this case, concatenation would lead to  
160 erroneous results (Scargle, 1989). Instead, at each time shift,  $\Delta$ , a proper “temporal mask” of  
161 flagged frames will be the intersection of the temporal mask at zero-lag and the shifted temporal  
162 mask. This implies that, for each time shift, the number of frames excluded from the covariance



163 computation exceeds the number of high-motion frames. Theoretically, this temporal masking  
164 strategy can lead to data loss by as much as a factor of two; however, in practice, the loss is  
165 less because high-motion frames tend to cluster together (PowerSchlaggar and Petersen,  
166 2015).

167 There are several ways to incorporate censoring into TDE (Fig. 2). One straightforward  
168 approach is simply to include, for each lag, all valid pairs of temporal samples as defined by the  
169 intersection temporal mask. Although this strategy makes use of all non-flagged frames, it can  
170 produce large differences in the number of frames contributing to each  $\Delta$  of the CCF (Fig. 2a,  
171 black). Consequently, the variance of each CCF point can differ substantially. Another concern  
172 is that motion artifacts may have temporally extended effects. Thus, while a pair of frames  
173 separated by a single high-motion time point may be valid, including them may corrupt the CCF  
174 at that  $\Delta$ .

175 An alternative strategy is to compute CCFs only over blocks of contiguous data (Fig. 2A,  
176 dark and light green), which avoids both above discussed limitations. We refer to this strategy  
177 as the "block approach." Summing (unnormalized) cross-covariance estimates across such  
178 blocks yields a single CCF for the time series (Eq. (6)). In prior analyses, we have used a  
179 conservative version of this approach, retaining only blocks of low-motion data at least 60  
180 seconds in duration (Mitra *et al.*, 2014). Head movements often are followed by prolonged  
181 signal changes (Power *et al.*, 2018). However, global signal regression (GSR) effectively limits  
182 motion artifacts to the epoch of movement (Power *et al.*, 2014; Byrge and Kennedy, 2018;  
183 Power *et al.*, 2018), which suggests that a 60-second minimum may be overly conservative  
184 *when using GSR*. Therefore, it is worthwhile to determine the degree to which including shorter  
185 blocks can reduce sampling error. To limit the degree to which different points of the CCF have  
186 unequal numbers of samples, a reasonable lower limit for block duration would be one that

187 allows for at least one sample per block to contribute to every point of the CCF (i.e.,  $(\Delta_{max} +$   
188  $1) \times TR$ ) (Fig. 2A, light green).

189         Given contiguous data, computing lagged CCFs raises the choice of normalizing the  
190 estimate at all lags by a constant (number samples at zero lag, as in Eq. 6) vs. normalizing by  
191 the number of samples at each lag. The first option leads to biased but lower variance estimates  
192 (Jenkins and Watts, 1968). Given non-contiguous data, as in the present case, the situation is  
193 more complicated as the number of samples at each lag may vary widely. Figure 2B illustrates  
194 this issue using surrogate data combined with the real temporal mask obtained from moderately  
195 censored data. This toy case demonstrates that normalization strategy can lead to markedly  
196 different TD estimates.

197         Finally, if the block approach (see above) is used, a single high-motion time point will  
198 result in the loss of several surrounding frames. Because BOLD fluctuations are very slow ( $<0.1$   
199 Hz), it is possible that a reasonably accurate value for a contaminated frame may be estimated  
200 from its surrounding frames. Thus, interpolation is another viable strategy for reducing  
201 excessive data loss, and hence, sampling error. Alternatively, this strategy assumes that  
202 surrounding frames are free of artifact, which is not necessarily true. As with small blocks,  
203 determining the utility of interpolation requires quantitative comparisons using real data.

### 204 **3. METHODS**

#### 205 *3.1. Subjects*

206         We used the recently published Midnight Scan Club (MSC) dataset comprising ten 30-  
207 minute eyes-open rsfMRI sessions from each of ten individuals (Gordon *et al.*, 2017).

#### 208 *3.2. MRI acquisition*

209         Details for acquisition of the MSC dataset have been described previously (Gordon *et*  
210 *al.*, 2017). All imaging was performed on a Siemens TRIO 3T MRI scanner. For each subject,

211 anatomical scans included four T1-weighted sagittal magnetization-prepared rapid gradient-  
212 echo (MP-RAGE) images as well as four T2-weighted sagittal images. Functional, T2\*-weighted  
213 imaging (gradient-echo, 36 slices, TR = 2.2 s, TE = 27 ms, flip angle = 90°, voxel size = 4 mm  
214 isotropic) included 30 contiguous minutes of resting-state fMRI, collected during each of ten  
215 sessions performed at midnight, giving each subject five hours of resting-state data. During  
216 resting-state data acquisition, subjects fixated a white crosshair against a black background. An  
217 EyeLink 1000 eye-tracking system (<http://www.sr-research.com>) indicated that one subject  
218 (MSC08) exhibited prolonged eye closures, likely indicating sleep (Gordon *et al.*, 2017).

### 219 *3.3. fMRI preprocessing*

220 For each subject a mean of field maps collected over multiple sessions was applied to  
221 images from all sessions for distortion correction, as described in detail elsewhere (Laumann *et al.*  
222 *et al.*, 2015; Laumann *et al.*, 2016).

223 Functional data were next preprocessed to reduce artifact, maximize cross-session  
224 registration, and transform to an atlas space. All sessions underwent correction for odd-even  
225 slice intensity differences stemming from interleaved acquisition of slices within a volume,  
226 correction for within-volume slice-dependent time shifts, intensity normalization to a whole brain  
227 mode value of 1000, and within- and between-run rigid body correction for head movement.  
228 Transformation to Talairach atlas space (Talairach and Tournoux, 1988) was computed by  
229 registering the mean intensity image from a single BOLD session via the average T1-weighted  
230 image and average T2-weighted image, and subsequent BOLD sessions were linearly aligned  
231 to this first session. This atlas transformation was combined with mean field distortion correction  
232 and resampling to 3 mm isotropic atlas space in a single step.

233 Subsequent processing was performed on the atlas-transformed, volumetric time series  
234 to further reduce artifact. First, temporal masks were created to flag motion-contaminated

235 frames. Such frames were identified by outlying values of framewise displacement (FD), a  
236 scalar index of instantaneous head motion, computed as the sum of the magnitudes of the  
237 differentiated translational (three) and rotational (three) motion parameters (Power *et al.*, 2012).  
238 Several subjects exhibited high-frequency peaks in the power spectrum of the  $y$  motion  
239 parameter, which captured the phase-encoding direction (anterior-to-posterior) (Gordon *et al.*,  
240 2017); because this did not have an obvious influence on the data, nor an obvious relationship  
241 to typical head movements, and occurred above frequencies of interest ( $>.1$  Hz), we low-pass  
242 filtered the  $y$ -motion time course at 0.1 Hz in all subjects prior to computing FD to prevent  
243 inflation of FD values and superfluous data loss (Siegel *et al.*, 2017). Frames with FD exceeding  
244 0.2 mm (Power *et al.*, 2014) were replaced via linear interpolation to yield continuous time  
245 series that could be filtered while mitigating the spread of motion artifact to surrounding frames  
246 (Carp, 2013). Interpolated BOLD time series, as well as motion parameters (HallquistHwang  
247 and Luna, 2013), were subsequently passed through a zero-phase second-order Butterworth  
248 band-pass filter ( $0.005 \text{ Hz} < f < 0.1 \text{ Hz}$ ) to mitigate scanner drift and high-frequency artifact.  
249 Note that the extended duration of MSC scans gives the opportunity to capitalize on lower  
250 frequencies than typically analyzed with fMRI.

#### 251 *3.4. Component-based nuisance regression*

252 Next, the filtered BOLD time series underwent a component-based nuisance regression  
253 approach incorporating elements of previously published methods (Behzadi *et al.*, 2007;  
254 PatriatMolloy and Birn, 2015). Substantial variance in cerebrospinal fluid (CSF) and white matter  
255 corresponds to physiological noise (e.g., CSF pulsations), arterial  $p\text{CO}_2$ -dependent changes in  
256  $T2^*$ -weighted intensity (Power *et al.*, 2018), and motion artifact. Because such spurious  
257 variance is widely shared with regions of interest in gray matter, time series extracted from  
258 these regions are often used for nuisance regression. While the mean signals from white matter  
259 and CSF are typically regressed from gray matter BOLD time series, regression of multiple

260 components comprising the nuisance signals has the potential to remove additional  
261 physiological variance (Behzadi *et al.*, 2007) and motion artifact (Muschelli *et al.*, 2014;  
262 PatriatMolloy and Birn, 2015) that has spatiotemporal structure differing from the mean signal.

263         Generation of component-based nuisance regressors proceeded as follows. Masks of  
264 white matter and ventricles were segmented using FreeSurfer (Fischl, 2012; DaleFischl and  
265 Sereno, 1999) and spatially resampled in register with the fMRI data. Voxels surrounding the  
266 edge of the brain are particularly susceptible to motion artifacts (Satterthwaite *et al.*, 2013; Yan  
267 *et al.*, 2013a); hence, a third nuisance mask was created for extra-axial (or “edge” (PatriatMolloy  
268 and Birn, 2015)) voxels by thresholding a temporal standard deviation image (tSD > 2.5%)  
269 (Behzadi *et al.*, 2007) that excluded the eyes and a dilated whole brain mask. Voxel-wise  
270 nuisance time series were dimensionally reduced as in CompCor (Behzadi *et al.*, 2007), except  
271 that the number of retained regressors, rather than being a fixed quantity, was determined  
272 independently for each of the three nuisance masks by orthogonalization of the covariance  
273 matrix and retaining components ordered by decreasing eigenvalue up to a condition number of  
274 30 (i.e.,  $\lambda_{min}$  must satisfy  $\lambda_{max}/\lambda_{min} > 30$ ). The retained components across all compartments  
275 formed the columns of a design matrix,  $X$ , along with six motion parameter time series.

276         The columns of  $X$  are likely to be substantially collinear. To prevent numerical instability  
277 owing to rank-deficiency during nuisance regression, a second-level singular value  
278 decomposition was applied to  $XX^T$  to impose an upper limit of 250 on the condition number.  
279 This strategy yielded on average  $29.6 \pm 8.5$  (mean  $\pm$  standard deviation) regressors per 30  
280 minute session (range = 16-55 regressors), to which the mean signal averaged over the whole  
281 brain (global signal), along with its first derivative, were added. Although global signal variance  
282 is in part neural in origin (Schölvinck *et al.*, 2010; Wong *et al.*, 2013; Liu *et al.*, 2018; Turchi *et*  
283 *al.*, 2018), global signal regression is a highly effective strategy to reduce spatially distributed  
284 artifact from myriad sources (Satterthwaite *et al.*, 2013; Power *et al.*, 2014; Ciric *et al.*, 2017;

285 Power *et al.*, 2017; Power *et al.*, 2018) as well as the temporally extended effects of such  
286 artifacts (Byrge and Kennedy, 2018; Satterthwaite *et al.*, 2013; Power *et al.*, 2014; Power *et al.*,  
287 2017), which could lead to spurious time delays.

288 The final set of regressors was applied in a single step to the filtered, interpolated BOLD  
289 time series. Finally, the interpolated time points were re-censored using a temporal mask. Time  
290 series were averaged within ROIs, which were either 264 10 mm diameter spheres (Power *et*  
291 *al.*, 2011) for TD and FC distributions or 6 mm gray matter cubes (Mitra *et al.*, 2014) for time  
292 delay matrices and lag projections maps (Fig. 1, 5 & 10).

### 293 3.5. Surrogate fMRI time series

294 Determination of TDE accuracy requires knowledge of the true delay between a pair of  
295 time series, which is not known in real fMRI data. Therefore, we simulated pairs of fMRI time  
296 series with modeled time delays. Characteristics of fMRI signals, such as their  $1/f$ -like behavior  
297 (ZarahnAguirre and D'Esposito, 1997; He *et al.*, 2010), very low frequencies of interest ( $< 0.1$   
298 Hz), and comparatively small time delays ( $\pm 1$  s), make TDE in fMRI a unique challenge. The  
299 creation of time series with these features proceeded as follows: First, two  $1/f^\alpha$  Gaussian noise  
300 time series of the desired length and temporal sampling rate were generated using a previously  
301 published algorithm for the frequency domain generation of power law noise signals (Kasdin,  
302 1995; Kasdin and Walter, 1992), as implemented in MATLAB (StoyanovGunzburger and  
303 Burkardt, 2011). We used  $\alpha = 0.7$  for all simulations, which is a typical value for this parameter  
304 in fMRI data despite small variations across the brain (He *et al.*, 2010; He, 2011). Next, these  
305 time series were put through the same bandpass filter as the BOLD data (i.e.,  $0.005 < f < 0.1$ ,  
306 2<sup>nd</sup> order Butterworth). To precisely specify the desired correlation, these time series were  
307 standardized (made zero-mean, unit-variance), orthogonalized by projection onto the  
308 eigenvectors of the desired  $2 \times 2$  correlation matrix  $R$ , standardized once more, and finally  
309 multiplied by an upper-triangular matrix  $U$  satisfying  $R = U^T U$  (obtained by the Cholesky

310 factorization of  $R$ ). This resulted in two zero-mean time series of unit variance that duplicated  
 311 the spectral content of BOLD time series and had the specified correlation at zero-lag. Finally,  
 312 one of the time series,  $x_1$ , was shifted in the frequency domain representation to precisely  
 313 model the desired time delay,  $\tau$ . Thus,

$$314 \quad x_{1,\Delta=\tau} = F^{-1}(F(x_{1,\Delta=0}) \cdot e^{-i2\pi f\tau}) \quad (10)$$

315 where  $F(x)$  and  $F^{-1}(x)$  are the Fourier and inverse Fourier transforms of  $x$ ,  $\Delta$  is the time shift,  $f$   
 316 is the equal-length sequence of frequency-domain samples, and multiplication is performed  
 317 elementwise. TDE was performed between the resulting time domain signal,  $x_{1,\Delta=\tau}$ , and its  
 318 unshifted signal pair,  $x_{2,\Delta=0}$ .

319 Except where noted, simulated time series were constructed with the following  
 320 parameters:  $r = 0.9$  (before time shifting),  $\tau = 0.5$  s, duration = 60 min. An unrealistically high  $r$   
 321 was used to visually enhance relationships between TDE error and other factors. Each data  
 322 point in Figures 3, S1, and S2 represents 2,000 simulations.

323 TDE accuracy was evaluated in terms of bias, variance, and root-mean-square error  
 324 (RMSE). Over  $n = 2,000$  simulations, these were computed as follows:

$$325 \quad Bias(\hat{\tau}) = \frac{1}{n} \sum_{i=1}^n \hat{\tau}_i - \tau \quad (11)$$

$$326 \quad Variance(\hat{\tau}) = \frac{1}{n} \sum_{i=1}^n (\hat{\tau}_i - \bar{\tau})^2 \quad (12)$$

$$327 \quad RMSE(\hat{\tau}) = \sqrt{\frac{1}{n} \sum_{i=1}^n (\hat{\tau}_i - \tau)^2} = \sqrt{Bias^2(\hat{\tau}) + Variance(\hat{\tau})}, \quad (13)$$

328 where  $\tau$ ,  $\hat{\tau}_i$  and  $\bar{\tau}$  signify the true time delay, the time delay measured on a given simulation  $i$ ,  
 329 and the mean time delay over  $n$  observations, respectively.

330 We additionally used zero-lag surrogate time series to evaluate FC accuracy. For these  
 331 simulations, the “true” correlation  $r$  was set in the above manner but for extended duration time  
 332 series (5,000 minutes). This allowed us to estimate the accuracy of  $\hat{r}$  computed over a range of  
 333 smaller data durations and a range of true correlation ( $r$ ) values. Accuracy was evaluated in  
 334 terms of RMSE:

$$335 \quad RMSE(\hat{r}) = \sqrt{\frac{1}{n} \sum_{i=1}^n (z(\hat{r}_i) - z(r))^2}, \quad (14)$$

336 where  $z()$  signifies Fisher z-transformation (Fisher, 1915; Fisher, 1921).

337 Finally, surrogate data were used to isolate the effects of censoring-induced sampling  
 338 variability (i.e., variable data *quantity*) from variable data *quality* and true intra- and inter-subject  
 339 variability (Figure 8C-D only). For this analysis, surrogate time series were generated as above  
 340 but were projected onto the eigenvectors of the real, group average  $264 \times 264$  correlation  
 341 matrix.

342 MATLAB code for comparing TDE strategies in surrogate time series and computing TD  
 343 matrices and weighted lag projections as in this paper has been made publicly available at [link  
 344 will be provided upon acceptance].

### 345 *3.6. Outcome metrics and statistical analysis*

346 TDE strategies (discussed in Section 2) may have opposing impacts on bias and  
 347 variance, making it difficult to determine whether one strategy is superior to another. However,  
 348 because the effects on bias and variance disproportionately impact high-motion data, our  
 349 primary outcome measures were 1) correspondence between low- and high-motion sessions  
 350 within each subject, and 2) correspondence between each session and the group average.  
 351 Correspondence was computed over all unique ROI pairs for both TD and FC matrices (i.e.,  
 352 vectorized upper triangular of the  $264 \times 264$  TD or FC matrix). TD pairs corresponding to  $|FC| <$



353 .2 (as determined by the censored group average FC matrix) were excluded in these  
354 comparisons to focus reliability analyses on more robust relationships. Correspondence was  
355 determined by Spearman's  $\rho$  for TD and Pearson's  $r$  for FC distributions.

356         Sampling error tends to result in larger magnitude correlations (PowerSchlaggar and  
357 Petersen, 2015), which increases the probability of the CCF (erroneously) exhibiting a maximum  
358 at some offset from zero-lag. Consequently, sampling error also tends to result in larger time  
359 delays. Therefore, we used the width of a given TD or FC distribution as a proxy for sampling  
360 error, which we computed as the standard deviation,  $\sigma$ , across the distribution. We also used  
361 QC:FC (Power *et al.*, 2012) and QC:TD correlation distributions to visualize the impacts of head  
362 motion and sampling error on correlations and time delays, respectively. Each data point in  
363 these distributions reflects the correlation between mean FD (quality control metric) and a  
364 specific ROI:ROI pair FC (or TD) value, across all 100 MSC sessions. We use the FC or TD  
365 absolute value ( $|FC|$  and  $|TD|$ ) in order to focus on the impact of sampling error on the  
366 magnitude of these statistics. While mean FD reflects the degree of head motion prior to  
367 censoring, it also provides an approximation for the relative amount of data loss following  
368 censoring (i.e., subjects with higher mean FD will generally lose more data due to censoring).  
369 Thus, because we are primarily interested in the effects of sampling variability due to data loss,  
370 we use mean FD computed *prior* to censoring throughout the paper. This is favorable to FD  
371 computed *after* censoring, which will be less correlated with data loss, and the actual quantity of  
372 data loss, which will differ depending on the strategy used for TDE. Nonetheless, FD computed  
373 before and after censoring correlated well ( $r = .71$ ). Moreover, across different strategies, FD  
374 computed prior to censoring correlated well with the number of frames used for TDE ( $r > -.75$  in  
375 all cases;  $r = -.92$  with minimum allowable block duration). Further information related to motion  
376 and censoring can be found in Supplementary Tables 1-4.

377 Statistical significance of differences between TDE methods was assessed with  
378 Student's paired t-tests performed on the Fisher-z transformed  $\rho$  or  $r$  values, or  $\sigma$  values  
379 corresponding to the TD or FC distributions.

## 380 4. RESULTS

### 381 4.1. Factors influencing TDE (and FC) accuracy: insights from surrogate time series

382 We used data simulations to explore the dependence of BOLD TDE accuracy on data  
383 quantity, correlation magnitude, and temporal sampling interval (Fig. 3). Figure 3A shows a  
384 roughly linear relationship between data quantity and RMSE extending over multiple decades  
385 on a log-log plot, underscoring the sensitivity of TDE accuracy to the quantity of data. Note that  
386 an unrealistically high correlation ( $r = 0.9$ ) was used to make the pattern clear; as is evident in  
387 Figure 3B, TD RMSE exhibits a strong dependence on correlation magnitude. In particular, as  
388 correlation magnitude falls below  $\sim 0.2$ , RMSE markedly increases. An algebraic model of this  
389 effect is given below in section 4.4. Thus, in real (GSR) data, where the mean pairwise  
390 correlation magnitude may be as low as  $\sim 0.1$  (as in the present study), the pattern in Figure 3A  
391 would be substantially shifted rightward (see Fig. S1 for RMSE plots at weaker correlation  
392 magnitudes). Note that Figure 3B explores TD RMSE as function of correlation magnitude in 60-  
393 minute time series; see Figure S1 for this dependence in typical session- (10 minutes) and  
394 group-level (250 minutes) data quantities.

395 In comparison to data quantity and correlation magnitude, the effect of TR is relatively  
396 minor but is most apparent given large quantities of data, where higher TRs (lower sampling  
397 rate) asymptote at greater RSME (Fig. 3A & S1). Thus, coarse sampling leads to poorer TDE  
398 resolution, even after parabolic interpolation. The improved detection of directionality in fMRI  
399 with increased sampling rate has previously been demonstrated in real data (Lin *et al.*, 2014).

400 As pointed out in Equation (13), RMSE can be expressed in terms of bias, which refers  
401 to the difference between the expected value of an estimator and the true value of the  
402 parameter being estimated, and variance, which reflects the expected (squared) deviation of a  
403 single estimate from the mean estimate across a given number of observations. In Figures 3A  
404 and B, separate bias and variance plots are not shown because RMSE is largely determined by  
405 the latter (i.e., there is no systematic bias in TDE associated with specific data quantities or  
406 correlation magnitudes). However, it is useful to visualize all three properties when exploring  
407 dependence of TDE accuracy on the true time delay relative to the sampling interval, which is  
408 shown in Figure 3C for multiple TRs. The sinusoidal bias pattern (Fig. 3C, left) is a well-known  
409 characteristic of parabolic interpolation (Boucher and Hassab, 1981; Céspedes *et al.*, 1995) and  
410 effectively biases estimates toward the nearest TR. This bias progressively worsens with  
411 increasing temporal distance from (roughly) the nearest half-multiple of the TR. Thus, for time  
412 delays in the range of 0 s up to 2 s for TR = 2 s, delays closer to 2 s are overestimated, and  
413 there is no bias at exactly 1 s. Bias is most severe when  $\tau/TR \approx 0.3$  and  $\approx 0.7$ , as reported  
414 previously (Boucher and Hassab, 1981; Céspedes *et al.*, 1995). This is yet another instance of a  
415 bias-variance tradeoff, as other TDE approaches (e.g., in the frequency domain) are free of this  
416 bias but exhibit greater variance.

417 A complementary pattern is observed for variance, which peaks halfway between  
418 samples (Boucher and Hassab, 1981; Céspedes *et al.*, 1995) (Fig. 3C, right). Combining these  
419 bias and variance effects yields an RMSE pattern that exhibits peaks around the quarter-interval  
420 marks and a local trough halfway between samples (Fig. 3C, lower). Note also that RMSE in  
421 seconds scales with TR without change in pattern (Céspedes *et al.*, 1995).

422 Like TDE, FC accuracy is highly dependent on data quantity and continues to decrease  
423 linearly on a log-log plot up to the maximum measured duration (1000 minutes). However, FC  
424 sampling variability is not obviously sensitive to the true correlation of a given time series pair,

425 nor the temporal sampling rate, making it a simple reflection of data quantity measured in units  
426 of time (Fig. S2).

#### 427 *4.2. Manifestations of bias and variance in real data (prior to censoring)*

428 We next sought to determine whether the above relationships are apparent in real data.  
429 Figure 4A displays histograms of all possible pairwise time delay estimates among 264 ROIs  
430 (Power *et al.*, 2011) using our published approach for TDE (Mitra *et al.*, 2014): data is from  
431 either one session (MSC01 session 1; red), one subject (MSC01, time delays averaged over all  
432 10 sessions; green), or all 10 subjects (MSC01-MSC10, time delays averaged across sessions  
433 within subject and subsequently across subjects; black). Decreasing variance associated with  
434 increasing data quantity is apparent in the widths of the distributions.

435 Figure 4B displays histograms of all unique pairwise time delays from all 100 MSC  
436 sessions. The blue trace reflects only those time delays corresponding to ROI pairs with zero-  
437 lag correlation magnitude  $\geq 0.2$ , while pairs with correlation  $< 0.2$  are represented by the pink  
438 trace. Several inferences can be made from these histograms. First, there are far more pairwise  
439 correlations below rather than above 0.2. Second, parabolic interpolation bias is much more  
440 apparent for weaker as opposed to stronger correlations. Structure in the pink trace (slope  
441 discontinuity at  $\pm 1.1$  sec in data acquired at TR = 2.2 sec) reflects bias associated with  
442 parabolic interpolation (Moddemeijer, 1991) (Fig. 3C, left). The pattern is less obvious (but  
443 nonetheless present) for more strongly correlated pairs (blue) because they exhibit less  
444 sampling error, hence, relatively few delays far from zero.

445 We next consider how TD error can obscure spatiotemporal patterns of interest. Figure  
446 1D shows the MSC-average TD matrix, masked to include only cortical (6 mm)<sup>3</sup> cubes with  
447 high-probability ( $\geq 90\%$ ) affiliation with one of seven functional networks (Hacker *et al.*, 2013).  
448 The rows and columns of this matrix have been sorted from early-to-late by their mean values,

449 and by functional network, to demonstrate delays on the order of  $\sim 1$  s in both on- and off-  
450 diagonal blocks. Note that the well-ordered, early-to-late progression within each block, as well  
451 as the consistency with which certain voxels appear as early or late across rows/columns, is not  
452 imposed; rather, this latency structure suggests that infra-slow activity is well-organized both  
453 within and between networks. Importantly, this matrix represents 3000 minutes of data and  
454 recapitulates prior findings obtained from similarly large data quantities (Mitra *et al.*, 2014). In  
455 contrast, Figure 5A shows a TD matrix from one MSC subject (MSC01, averaged across all 10  
456 sessions; 300 minutes) following the same sorting procedure as in Figure 1D, along with the  
457 zero-lag, absolute value FC matrix from the same subject. Structure in the off-diagonal blocks is  
458 less evident in Figure 5A in comparison to Figure 1D. In general, the degree to which a block in  
459 the TD matrix of Figure 5A is structured appears to correspond to the strength of absolute value  
460 FC within the block.

461 To quantify the relationship between TD matrix structure and correlation magnitude, we  
462 first created a measure that approximately reflects temporal structure. Specifically, because  
463 well-structured blocks of the sorted TD matrix appear to comprise roughly iso-latent diagonals,  
464 we defined “error” in the latency structure of each block as the RMSE of all time delays in the  
465 block relative to the mean delay of their respective diagonals (Fig. 5B). Next, we averaged  $|FC|$   
466 within each of the blocks (Fig. 5C). These procedures resulted in block-wise values of both error  
467 and mean  $|FC|$  (Fig. 5D), which we correlated with each other using session-, subject-, and  
468 group-level matrices. As expected, error in latency structure decreased with increasing data.  
469 Moreover, there was a strong inverse correlation between error and mean  $|FC|$  at the session ( $r$   
470  $= -.87$ ,  $p < .0001$ ) and subject ( $r = -.81$ ,  $p < .0001$ ) levels, but not at the group level ( $r = .26$ ,  $p =$   
471  $.18$ ) ( $N = 28$  blocks for each correlation) (Fig. 5E). This pattern is understandable as a  
472 consequence of Figure 3A-B: while data quantity at the group-level was sufficient for a majority  
473 of ROI pairs (e.g., Fig. 1D), data quantity contributing to session- and subject-level TD matrices

474 was sufficient for only those ROI pairs with relatively strong FC. Once sampling error is largely  
 475 mitigated, there is little dependence of latency structure on the underlying correlations.

#### 476 4.3. Sampling error incurred from motion censoring

477 As TDE sampling error can be readily observed prior to censoring, removing time points  
 478 necessarily increases this source of error, even while mitigating error stemming from artifact.  
 479 Accordingly, we sought to determine how censoring contributes to sampling error. Because  
 480 sampling error tends to increase the magnitude of correlations (Yan *et al.*, 2013a;  
 481 PowerSchlaggar and Petersen, 2015), and thus, cross-correlation derived time delays (e.g., Fig.  
 482 4), we focused on TD and FC magnitudes and distribution widths in relation to head motion and  
 483 data loss.

484 Results pertaining to head motion artifact and data loss are shown in Figure 6. Prior to  
 485 motion censoring, the standard deviation of a single session's TD distribution was positively  
 486 correlated with mean FD across all 100 MSC sessions ( $r = .32, p < .001$ ) (Fig. 6A left). This  
 487 result implies that head motion introduces spurious time delays that tend to be longer than those  
 488 arising from neurophysiology (Byrge and Kennedy, 2018). After censoring  $FD > 0.2$  mm frames  
 489 (Power *et al.*, 2014) and using our original strategy of discarding segments of data  $< 60$  s in  
 490 duration (Mitra *et al.*, 2014), the mean distribution width (as measured by the standard  
 491 deviation) across all sessions was greatly increased ( $\sigma_{pre} = 1.60 \pm 0.07, \sigma_{post} = 1.67 \pm 0.15; p_{post-}$   
 492  $pre < .0001$ ) and the correlation between TD distribution width and mean FD increased to  $.72 (p <$   
 493  $.0001)$  (Fig. 6A right). Although the standard deviation of the FC distribution was inversely  
 494 correlated with mean FD prior to censoring ( $r = -.44, p < .0001$ ), perhaps owing largely to  
 495 stronger negative correlations in low-motion sessions, FC  $\sigma$ , like TD  $\sigma$ , also became strongly  
 496 correlated with mean FD after censoring ( $r = .43, p < .0001$ ) ( $\sigma_{pre} = 0.18 \pm 0.01, \sigma_{post} = 0.20 \pm$   
 497  $0.03; p_{post-pre} < .0001$ ) (Fig. 6B).

498 Relating distribution widths to FD before versus after censoring, as above, permits  
499 quantification of the influence of head motion and data loss, respectively, on TD (and FC) at the  
500 session level. These relationships can be further examined at the level of individual ROI pairs.  
501 Accordingly, a histogram may be constructed in which each observation reflects one ROI pair,  
502 and its value corresponds to the correlation, across 100 sessions, between mean FD and the  
503 TD of that ROI pair. A similar histogram can be constructed for FC for all ROI pairs. Such  
504 “QC:FC” (quality control:functional connectivity) correlation distributions have previously been  
505 used to visualize the impact of head motion on FC, where head motion generally shifts the  
506 QC:FC distribution rightward (Power *et al.*, 2014; Ciric *et al.*, 2017). Here, we extend this  
507 strategy to studying how head motion (and data loss) impacts TD as well as FC. We computed  
508 QC:TD (QC:FC) by taking the absolute value of the TD (FC). pair to focus specifically on  
509 sampling error. A null model was generated by randomly permuting mean FD over sessions.  
510 Prior to censoring, the QC:|TD| distribution was shifted slightly rightward compared to the null  
511 model (Fig. 6C) while the QC:|FC| distribution was shifted leftward (Fig. 6D). Thus, as observed  
512 at the session level (Fig. 6A-B), head motion leads to inflated estimates of TD while tending to  
513 reduce FC magnitude. After censoring, both QC:|TD| and QC:|FC| distributions were shifted  
514 rightward, suggesting, once again, that increased data loss leads to inflated TD and FC  
515 estimates. Altogether, these findings point to a strong increase in sampling error associated with  
516 censoring under the 60-second block requirement.

517 We next explored the ramifications of censoring-induced sampling error. Because high-  
518 motion sessions are more severely impacted, we assessed correspondence between the five  
519 lowest- and highest-motion sessions within each of the 10 MSC subjects, as well as the  
520 correspondence of each session to the group average. Importantly, the latter metric is also  
521 sensitive to head motion and is significantly inversely correlated with mean FD across all 100  
522 sessions before motion censoring ( $r = -.39$ ,  $p < 0.0001$  for TD;  $r = -.39$ ,  $p < 0.0001$  for FC).

523 Comparing TDE results with and without motion censoring, using an FD threshold of 0.2 mm  
524 with the 60 second block requirement, resulted in greater divergence between low- versus high-  
525 motion sessions (N = 10 subjects,  $p < .05$ ) and consistently decreased session-to-group  
526 correspondence (N = 100,  $p < .001$ ) (Fig. 6D). This was true of FC as well (low:high-motion,  $p <$   
527 0.1; session:group,  $p < 0.001$ ) (Fig. 6E). Thus, an overly stringent approach to motion censoring  
528 (FD < 0.2mm and 60 sec blocks) yields poorer results for both TD and FC than simply retaining  
529 the high-motion time points.

#### 530 4.3. Comparing strategies for TDE among discontinuous time series

531 The 60-second block duration was originally adopted to avoid TDE errors generated by  
532 temporally extended artifact associated with head motion. However, it has since been shown  
533 that GSR (which we use) effectively reduces such artifacts (Power *et al.*, 2014; Byrge and  
534 Kennedy, 2018), Accordingly, we next determined how including relatively short epochs impacts  
535 our outcome metrics. Outcome was again assessed as the correlation between vectorized TD  
536 and FC matrices (correspondence). We found that low:high-motion correspondence as well as  
537 session:group correspondence monotonically increased as the imposed minimum block  
538 duration was reduced down to the limit consistent with at least one data point from each block  
539 contributing to each CCF lag ("minimum allowable" block duration) (Fig. 7A). Similar results  
540 were observed for FC (Fig. 7B).

541 Results so far have been reported for the unbiased CCF estimator, i.e., normalized by the  
542 number of sampled frames at each lag. Since the minimum allowable block approach ("min")  
543 proved optimal, we compared it against three alternatives: (i) biased CCF estimator (i.e.,  
544 normalized by the number of sampled frames at zero-lag) with the minimum allowable block  
545 duration ("biased"), (ii) enforcing equal samples at each time point in an unbiased CCF  
546 estimator (as in Figure 2A, light green; "equal"), and (iii) unbiased estimator using all valid  
547 frames at a given time shift (as in Figure 2A, black; "all"). Of these 4 approaches, the unbiased



548 CCF estimator with minimum allowable block requirement performed best (Fig. S3). However,  
549 the differences between these approaches were minimal in comparison to relaxing the imposed  
550 minimum block duration requirement.

551 We additionally investigated whether interpolating over censored frames could further  
552 improve the unbiased, minimum allowable block approach. Given the degree of sampling error  
553 present at the single-session level, even with 30-minute sessions, it might be expected that  
554 interpolation would improve outcome metrics by salvaging data, even if that data is of poor  
555 quality. Accordingly, the effects of linear interpolation were compared against an approach in  
556 which interpolated frames were replaced with the original (post-regression), potentially  
557 contaminated values. Although both of these approaches improved group correspondence for  
558 both TD and FC, interpolation did not outperform the alternative for FC and, for TDE, performed  
559 significantly worse (Fig. S4).

560 Finally, because the minimum allowable block duration approach is far more lenient than  
561 the imposed 60-second minimum and is comparable with conventional FC data constraints  
562 (e.g., (Power *et al.*, 2014)), we repeated the analyses in Figure 6A-D using the minimum  
563 allowable block duration approach. We found that both TD distribution widths and magnitudes  
564 remained positively correlated with mean FD, though these relationships were no longer  
565 apparent for FC (Fig. 8). In order to aid interpretation of this result, we repeated these analyses  
566 in surrogate time series; doing so enabled us to isolate potential consequences of censoring-  
567 induced sampling error, when using the minimum allowable block duration, from effects related  
568 to data quality or biology. We generated a single set of 264 surrogate time series based on the  
569 real group average correlation matrix (and assumption of zero lag among all time series). Next,  
570 we censored these time series according to the real temporal censoring masks ( $FD > 0.2$ ) from  
571 each of the 100 MSC sessions. Hence, any differences in correlation or lag structure computed  
572 from these time series would be attributable to censored-induced sampling error.

573 We found TD and FC relationships with FD to be outstanding in the surrogate data (Fig.  
 574 9), demonstrating that censoring-induced sampling variability remains a significant source of  
 575 error for both TD and FC when using the minimum allowable block duration approach, despite  
 576 30-minute sessions. Taking these findings into account, it can be concluded from the real data  
 577 (Fig. 8) that 1) sampling variability still has a considerable influence on observed time delays  
 578 when using minimum allowable block duration, and 2) absence of a prominent FC:FD  
 579 relationship when using the minimum block approach does not indicate the absence of sampling  
 580 error, but rather that the influence of sampling error is less salient in comparison to other factors  
 581 (e.g., data quality and inter-session or inter-subject variability). Thus, sampling error remains an  
 582 issue for TD and FC when using 30-minute sessions.

#### 583 *4.4. Weighting lag projections against sampling error*

584 We use “lag projections” to visualize each region’s mean temporal relationship with the  
 585 rest of the brain (Fig. 1E). Lag projections are computed by averaging a region’s temporal lag  
 586 with respect to all other regions (columns of TD matrices; Eq. 9). Given the dependence of TDE  
 587 accuracy on correlation, we asked whether this relation could be used to obtain more reliable  
 588 lag projections. Inspection of the relation between RMSE and  $|r|$  (e.g., Fig. 3B) suggested the  
 589 following functional form:

$$590 \quad f(r) = \beta \tan\left(\frac{\pi}{2}(1 - |r|)\right), \quad (15)$$

591 which accurately describes TD RMSE in surrogate time series with  $\beta$  fit by conventional  
 592 regression (Fig. 10A). This expression explains  $>.99$  of the variance in data quantities that are  
 593 typical in group-level analyses.

594 Equation (15) can be used to reduce the sampling error of lag projections by down-  
 595 weighting high-variance lag estimates. Thus, weighted lag projections, ( $wTD_p$ ) are computed by  
 596 inversely weighting TD pairs in proportion to modeled squared error. Thus,

$$597 \quad wTD_p = \left[ \frac{1}{\sum w_j} \right] \cdot \left[ \sum_{j=1}^n w_{1,j} \cdot \hat{t}_{1,j} \dots \sum_{j=1}^n w_{n,j} \cdot \hat{t}_{n,j} \right], \quad \text{where } w_{i,j} = \frac{1}{f^2(\hat{t}_{i,j})}. \quad (16)$$

598 In Equation (16), the correlation used to compute  $w_{i,j}$  is the conventional zero-lag FC metric  
 599 ( $\hat{r}_{i,j}$ ). In principle, the peak correlation at  $\hat{t}_{1,j}$  could have been used instead. However, this  
 600 measure is more susceptible to spurious inflation (BrightTench and Murphy, 2017). Given the  
 601 predominance of frequencies below 0.1 Hz in BOLD signals, zero-lag correlation differs only  
 602 slightly from peak correlations obtained within the range of lags studied here.

603 The effect of weighting in real data is examined in Figure 10B-D. Panel B shown voxel-  
 604 wise lag projections at the session-, subject- and group-levels. Weighting generally increases  
 605 the magnitude of projection values. This effect is quantitatively demonstrated in panel C as an  
 606 increase in session-level lag projection distribution widths. Weighting disproportionately impacts  
 607 sessions with less data (i.e., those with the higher mean FD), which manifests as greater  
 608 correlation between lag projection  $\sigma$  and FD (unweighted  $r = .75$ , weighted  $r = .37$ ). Despite this  
 609 effect, weighting drastically improved individual correspondence with the group average  
 610 *unweighted* lag projection (panel D). Thus, weighting effectively reduces the impact of sampling  
 611 error on the spatiotemporal patterns reflected in lag projections.

## 612 5. DISCUSSION

613 Here we have investigated factors contributing to sampling variability in fMRI time delay  
 614 estimation (TDE). The overarching result is that sampling error is a critical issue in both TDE  
 615 and zero-lag functional connectivity (FC) analyses. Below we discuss the implications of these  
 616 findings for rsfMRI research.

### 617 5.1. Motion censoring and TDE

618 We compared multiple strategies for TDE in the presence of discontinuities introduced  
619 from motion censoring (Fig. 2). Several of these strategies involve tradeoffs between bias and  
620 variance that more strongly impact high-motion sessions, i.e., sessions with less useable data.  
621 Therefore, to examine bias-variance tradeoffs, we used correspondence between low- and high-  
622 motion sessions as well as session-level correspondence with the motion-censored group data  
623 as outcome measures.

624 We found that including small blocks of contiguous data greatly reduces sampling error,  
625 down to the minimum allowable duration at which each block still contributes at least one  
626 temporal sample to all CCF lags (Fig. 7). Hence, in order to minimize data loss, the smallest  
627 possible number of time shifts should be used to estimate the CCF. Because the spectral  
628 content of BOLD signals is weighted towards very low frequencies, CCF peaks on the order  $\sim 10$   
629 sec or more may be expected. However, we currently exclude delays longer than four seconds  
630 as, in our experience, such latencies seem to reflect sampling error or artifact. Thus, in the MSC  
631 data, we were able to compute each CCF over just seven time shifts ( $\Delta_{max} = 3$ ), making the  
632 minimum allowable block duration  $(\Delta_{max} + 1) \times TR = 8.8$  s (see Section 2.2 and Fig. 2A).

633 Including all valid frames at a given time shift makes maximal use of data, hence  
634 minimized sampling error. However, this approach did not improve outcome measures, possibly  
635 owing to artifact in extremely short segments of data (i.e., here,  $< 5$  frames) that are surrounded  
636 by high-motion epochs, or spurious time delays associated with data samples on opposite sides  
637 of high-motion epochs. Because the "all" valid frames approach yields results comparable to the  
638 minimum allowable block approach ("min"), we favor the latter to avoid large disparities in the  
639 number of frames contributing to (and thus, the variance of) each lag of the CCF. Using a block  
640 approach, temporal interpolation also salvages substantial data, that is, frames surrounding the  
641 censored artifact. However, interpolation failed to improve outcome metrics beyond simply

642 including the original high-motion time points. Therefore, replacing potentially contaminated  
643 frames with interpolated data is not advisable. However, we did not account for the level of head  
644 motion in the frames that were interpolated. It remains possible that interpolation is useful in  
645 specific situations, for example, when a long block of data is interrupted by a single large head  
646 movement. Nonetheless, because we find that the minimum imposed block duration can be  
647 brief, interpolation, even if effective, has only limited potential to salvage data. Finally, we found  
648 that, while the biased CCF is associated with reduced variance, in our case, the unbiased CCF  
649 estimator yielded more favorable outcome metrics, although these differences were small.  
650 Based on these findings, the unbiased, minimum allowable block approach with no interpolation  
651 was the most effective of the examined TDE strategies.

652         We note that the purpose of these comparisons is primarily to outline the nuances of  
653 motion censoring in the context of TDE and to assess the involved bias-variance tradeoffs. In  
654 practice, the nature of the dataset (e.g., TR, degree and pattern of head motion, pre-processing  
655 strategies) will likely affect which approaches appear “optimal.” For example, interpolation may  
656 be more useful in datasets with shorter TR. Further, even micro-movements (i.e., FD below 0.2)  
657 can still have a detectable influence on rsfMRI data (Power *et al.*, 2014), and are likely to be  
658 more prevalent in temporal proximity to larger movements. Therefore, in very large datasets in  
659 which sampling error has been minimized, more aggressive data exclusion (e.g., stricter criteria  
660 for censoring and/or minimum block duration) may prove beneficial. Our findings may provide a  
661 useful guideline but are not guaranteed to be optimal in all cases. To aid in the evaluation and  
662 application of TDE in diverse fMRI datasets, we have made publicly available MATLAB code for  
663 lag computation in real and surrogate data as described here ([link will be made available upon  
664 acceptance]).

665 *5.2. Using correlation to inform lag analysis*

666           The accuracy of TDE between two signals is highly dependent on the strength of  
667 correlation between them (Walker and Trahey, 1995; CéspedesOphir and Alam, 1997) (Fig.  
668 3B). TD matrices comprise both intra- (on-diagonal) and inter-network (off-diagonal)  
669 relationships (e.g., Fig. 5), the latter of which correspond (by definition) to comparatively weak  
670 correlations prone to sampling error. Even so, large quantities of data reveal structure in off-  
671 diagonal blocks (Fig. 1D), suggesting that the activity shared between networks, albeit  
672 comparatively minor, is well-organized and may be biologically important (Mitra and Raichle,  
673 2016; Mitra and Raichle, 2018). Indeed, inter-network lag relationships may reflect integrative  
674 aspects of spontaneous brain activity complementary to the segregated functional networks  
675 revealed by zero-lag FC. Unfortunately, inter-network lag relationships require large quantities  
676 of data to estimate accurately (Fig. 5). Nonetheless, informative lag analyses can be performed  
677 with data quantities that may not be sufficient to stabilize the full TD matrix. For example, time  
678 delays among highly correlated ROI pairs can be estimated to reasonable accuracy with far less  
679 data than that required to study brain-wide propagation. Correlations may also be used to  
680 threshold seed lag maps, providing a more reliable visualization of the seed's temporal  
681 relationships with regions exhibiting closely shared activity.

682           TD matrices exhibit significant transitivity (Mitra *et al.*, 2014), as defined by the high  
683 proportion of all possible triples whose time delays sum to 0 (Nikolić, 2007), despite high  
684 dimensionality (Mitra *et al.*, 2015a). Thus, one-dimensional lag projections provide a useful  
685 spatiotemporal representation of propagation structure. Moreover, unlike full TD matrices, stable  
686 lag projections can be computed with relatively limited quantities of data (Fig. 10D). Further,  
687 statistical testing performed between lag projections from different groups or conditions is a  
688 useful low-dimensional approach to identifying regions whose spatiotemporal relationships may  
689 be altered (Mitra *et al.*, 2015b; Mitra *et al.*, 2017). By using correlation magnitude to give weight

690 to stronger pairwise relationships, weighted lag projections offer increased reliability and may  
691 prove more sensitive to group differences in spatiotemporal patterns.

692 We show above that sampling error increases the distribution widths of both measured  
693 TDs and correlations. Perhaps counterintuitively, weighting also increased the distribution width  
694 of lag projection values (Fig. 10C). Weighting likely increases sampling error by reducing the  
695 effective number of ROIs over which the mean temporal delay is computed, which leads to  
696 increased correlation between distribution width and data loss. However, this effect appears to  
697 be less important than down-weighting sampling error from weak correlations. Accordingly, the  
698 overall effect of weighting is improved reliability. We conclude that weighting usefully mitigates  
699 the adverse impact of sampling error on observed spatiotemporal topographies.

700 Finally, in addition to their statistical relation, TD and FC are phenomenologically related.  
701 Therefore, statistical differences in TD cannot be properly interpreted without comparison of  
702 underlying correlation structure. Likewise, interpretation of a given TD is greatly informed by  
703 knowledge of FC. Statistical significance of TD may be established by comparison with TD  
704 computed from appropriate null data: surrogate time series matching the quantity, correlation  
705 magnitude(s), TR, and auto- and cross-spectral content of the real data, but with peak  
706 correlation at zero-lag (i.e., devoid of latencies). This can be achieved, for example, by  
707 destroying phase information from the original time series (Hindriks *et al.*, 2018). Null data may  
708 also be used to construct confidence intervals for empirical TD. Nonetheless, the biological  
709 interpretation of a significant TD or significant between-group difference in TD may differ widely  
710 depending on the underlying FC, or the presence and/or nature of a change in FC.

### 711 *5.3. Motion censoring and sampling error in rsfMRI*

712 Limited data quantity is among the most significant challenges in rsfMRI research. The  
713 slow nature of fMRI signals (<0.1 Hz) necessitates large quantities of data to obtain sufficient

714 independent temporal samples. Even after reducing the minimum imposed block duration to that  
715 of conventional FC analysis (e.g., (Power *et al.*, 2014)), across 100 scans, the width of both the  
716 TD (in real and simulated data) and zero-lag FC (in simulated data) distributions following  
717 censoring remained positively correlated with head motion (i.e., data loss) (Fig. 8-9). Yan et al.  
718 previously demonstrated an increase in observed FC magnitude with excessive censoring (Yan  
719 *et al.*, 2013a); we show that this manifestation of FC sampling error is observable even in  
720 atypically long (30 minutes before censoring) rsfMRI time series.

721         We additionally found that QC:|TD| (in real and simulated data) and QC:|FC| (primarily in  
722 simulated data) distributions were shifted rightward after censoring, again reflecting the  
723 tendency of sampling error to inflate TD and FC estimates (Fig. 6C-D, Fig. 8B & Fig. 9B). Why  
724 have these patterns not been apparent in prior studies? One reason is that the range of data  
725 quantities in the present study is larger than typical. Thus, if 10 minutes typically are acquired,  
726 and censoring removes as much as half, the range of retained data quantities in a given dataset  
727 remains relatively limited. This potential for censoring to introduce large discrepancies in  
728 retained data quantity among long scans was previously discussed by Satterthwaite et al.  
729 (Satterthwaite *et al.*, 2013). Computing QC:|FC| rather than QC:FC, as in prior work, also is  
730 crucial. In our analysis, the QC:|FC| distribution was left-shifted (relative to the null) prior to  
731 censoring and right shifted after censoring (Fig. 6D). In contrast, the QC:FC distribution was  
732 zero-centered and minimally impacted by censoring (Fig. S5), which is typical of GSR data  
733 (Power *et al.*, 2014; Ciric *et al.*, 2017).

734         How does unequal sampling error impact statistical comparisons across groups?  
735 Welch's *t*-test and non-parametric tests for group differences in mean value take sampling  
736 variability into account. Thus, unequal sampling error is not a significant barrier in most group  
737 comparisons when group differences in mean value is at issue. The possibility of adjusting  
738 censoring (or discarding data) to ensure uniform number of frames in all subjects has been



739 discussed (Ciric *et al.*, 2017; Power *et al.*, 2014). However, we see no reason to deliberately  
740 introduce sampling error in this manner except when unequal variance biases outcomes, as in  
741 analyses based on machine learning (Power *et al.*, 2014). Of greater consequence is that  
742 sampling error is not fully eliminated in 30-minute rsfMRI sessions, let alone conventional five-  
743 minute sessions. This point is evident in recent reports on highly-sampled individuals, in which it  
744 is shown that single-subject FC matrix reliability plateaus only after more than an hour of data is  
745 analyzed (Laumann *et al.*, 2015; Gordon *et al.*, 2017).

746           Corruption of FC by head motion artifact and denoising strategies (e.g., nuisance  
747 regression, filtering) for reducing this motion-related bias have been well-described  
748 (PowerSchlaggar and Petersen, 2015; Satterthwaite *et al.*, 2017). However, these strategies  
749 currently fall short of completely removing motion artifact; hence, excluding high-motion time  
750 points further improves data quality (Power *et al.*, 2012; Power *et al.*, 2014; Satterthwaite *et al.*,  
751 2013; Yan *et al.*, 2013a; Yan *et al.*, 2013b; Burgess *et al.*, 2016; Ciric *et al.*, 2017; Siegel *et al.*,  
752 2017). But, motion censoring exacerbates sampling error (Ciric *et al.*, 2017). Although in  
753 principle sampling error (variance) is preferable to a systematic bias, sampling error increases  
754 the likelihood of spurious findings, reduces statistical power for detecting true effects, and  
755 produces artificially inflated estimates of TD and FC under the limited data conditions typical of  
756 most fMRI studies. Thus, censoring necessarily involves a bias-variance tradeoff, both sides of  
757 which should be considered when determining censoring criteria and when interpreting reported  
758 outcomes.

759           We used reliability to assess the tradeoff between bias reduction versus increased  
760 variance associated with censoring. Theoretically, reliability as an outcome measure can be  
761 confounded by reliable artifact. However, this is unlikely a significant concern in the present  
762 study for the following reasons: (1) We examined reliability following extensive nuisance  
763 regression. (2) Reliability was assessed as correspondence between low- and high-motion

764 sessions. (3) Reliability additionally was assessed as correspondence between individual  
765 sessions and the censored group average, and this measure inversely correlated with head  
766 motion. Thus, these measures were unlikely to have reflected reliability of artifact.

767 That said, we observed only modest and mixed effects of censoring on TD and FC  
768 reliability, provided that the analyses used the minimum allowable block duration strategy  
769 (compare Fig. 7 with Fig. 6E-F). The small magnitude of these effects may be attributable to  
770 effective denoising, including component-based regression (Behzadi *et al.*, 2007; PatriatMolloy  
771 and Birn, 2015) and GSR (Power *et al.*, 2014), and to the present dataset being relatively low-  
772 motion (Tables S1-4). The impact of censoring on reliability likely depends on both data quantity  
773 and quality, including the efficacy of pre-processing and the type and pattern of motion artifact  
774 (e.g., small vs. large, sparse vs. frequent; see Supplementary Tables 1-4 for session-specific  
775 information related to motion and censoring from the present dataset). More work is needed to  
776 better define these dependencies.

777 More generally, while many of the analyses herein suggest that maneuvers increasing  
778 data quantity are preferable, this was not always the case. As described above, neither the “all”  
779 condition nor temporal interpolation improved outcome measures despite increased data  
780 quantity. It is likely that an increase in bias associated with these approaches counteracted any  
781 benefits of decreased variance. Moreover, the present results focus on single sessions (albeit  
782 30 minutes); in larger group analyses, researchers can afford to sacrifice more potentially-  
783 biased data without substantially increased variance. Our analyses bring attention to the  
784 perhaps underappreciated influence of sampling error. In all cases, both artifact-related bias  
785 (Power *et al.*, 2012; Satterthwaite *et al.*, 2012; Van DijkSabuncu and Buckner, 2012; Siegel *et*  
786 *al.*, 2017) and sampling variability warrant careful consideration in fMRI analyses.

787  
788 **6. CONCLUSIONS**

789 TDE is a useful complement to zero-lag FC for studying the spatiotemporal organization  
790 of spontaneous infra-slow brain activity, as manifest in rsfMRI signals. However, sampling error  
791 presents a significant hurdle to TDE in fMRI and, as we show here, is an underappreciated  
792 challenge to FC analysis as well. Different research questions will warrant different tolerances  
793 for artifact-related bias and for sampling variability, each of which can often be reduced at the  
794 cost of increasing the other. In general, more data is needed for TDE as compared to zero-lag  
795 FC analysis, which itself requires more data than task-based fMRI analyses. Nonetheless, while  
796 large datasets will permit the most informative studies of propagation throughout the brain,  
797 useful lag projection comparisons and time delays between strongly-correlated time series can  
798 be computed with more limited quantities of data. Surrogate time series may be useful to gauge  
799 the data requirements for a specific question given the nature of the data.

#### 800 **ACKNOWLEDGEMENTS**

801 This work was supported by the NIH via NS080675 to M.E.R. and A.Z.S. and MH106253  
802 to A.M., and by the NSF via DGE-1745038 to R.V.R. We thank Nico Dosenbach for access to  
803 the MSC dataset (Gordon *et al.*, 2017).

## REFERENCES

- 804  
805
- 806 Amemiya, S., Takao, H., Hanaoka, S. and Ohtomo, K. (2016) 'Global and structured waves of  
807 rs-fMRI signal identified as putative propagation of spontaneous neural activity', *Neuroimage*,  
808 133, pp. 331-340.
- 809 Behzadi, Y., Restom, K., Liau, J. and Liu, T. T. (2007) 'A component based noise correction  
810 method (CompCor) for BOLD and perfusion based fMRI', *Neuroimage*, 37(1), pp. 90-101.
- 811 Biswal, B., Yetkin, F. Z., Haughton, V. M. and Hyde, J. S. (1995) 'Functional connectivity in the  
812 motor cortex of resting human brain using echo-planar MRI', *Magn Reson Med*, 34(4), pp. 537-  
813 41.
- 814 Boucher, R. E. and Hassab, J. C. (1981) 'Analysis of discrete implementation of generalized  
815 cross correlator', *IEEE T Acoust Speech*, ASSP-29(3), pp. 609-611.
- 816 Bright, M. G., Tench, C. R. and Murphy, K. (2017) 'Potential pitfalls when denoising resting state  
817 fMRI data using nuisance regression', *Neuroimage*, 154, pp. 159-168.
- 818 Burgess, G. C., Kandala, S., Nolan, D., Laumann, T. O., Power, J. D., Adeyemo, B., Harms, M.  
819 P., Petersen, S. E. and Barch, D. M. (2016) 'Evaluation of Denoising Strategies to Address  
820 Motion-Related Artifacts in Resting-State Functional Magnetic Resonance Imaging Data from  
821 the Human Connectome Project', *Brain Connect*, 6(9), pp. 669-680.
- 822 Byrge, L. and Kennedy, D. P. (2018) 'Identifying and characterizing systematic temporally-  
823 lagged BOLD artifacts', *Neuroimage*, 171, pp. 376-392.
- 824 Caballero-Gaudes, C. and Reynolds, R. C. (2017) 'Methods for cleaning the BOLD fMRI signal',  
825 *Neuroimage*, 154, pp. 128-149.
- 826 Carp, J. (2013) 'Optimizing the order of operations for movement scrubbing: Comment on  
827 Power et al', *Neuroimage*, 76, pp. 436-8.
- 828 Ciric, R., Wolf, D. H., Power, J. D., Roalf, D. R., Baum, G. L., Ruparel, K., Shinohara, R. T.,  
829 Elliott, M. A., Eickhoff, S. B., Davatzikos, C., Gur, R. C., Gur, R. E., Bassett, D. S. and  
830 Satterthwaite, T. D. (2017) 'Benchmarking of participant-level confound regression strategies for  
831 the control of motion artifact in studies of functional connectivity', *Neuroimage*, 154, pp. 174-  
832 187.
- 833 Céspedes, I., Huang, Y., Ophir, J. and Spratt, S. (1995) 'Methods for estimation of subsample  
834 time delays of digitized echo signals', *Ultrason Imaging*, 17(2), pp. 142-71.
- 835 Céspedes, I., Ophir, J. and Alam, S. K. (1997) 'The combined effect of signal decorrelation and  
836 random noise on the variance of time delay estimation', *IEEE T Ultrason Ferr*, 44(1), pp. 220-  
837 225.
- 838 Dale, A. M., Fischl, B. and Sereno, M. I. (1999) 'Cortical surface-based analysis. I.  
839 Segmentation and surface reconstruction', *Neuroimage*, 9(2), pp. 179-94.
- 840 Damoiseaux, J. S., Rombouts, S. A., Barkhof, F., Scheltens, P., Stam, C. J., Smith, S. M. and  
841 Beckmann, C. F. (2006) 'Consistent resting-state networks across healthy subjects', *Proc Natl  
842 Acad Sci U S A*, 103(37), pp. 13848-53.
- 843 Fischl, B. (2012) 'FreeSurfer', *Neuroimage*, 62(2), pp. 774-81.
- 844 Fisher, R. A. (1915) 'Frequency distribution of the values of the correlation coefficient in samples  
845 from an indefinitely large population', *Biometrika*, 10(4), pp. 507-521.
- 846 Fisher, R. A. (1921) 'On the "probable error" of a coefficient of correlation deduced from a small  
847 sample', *Metron*, 1, pp. 3-32.
- 848 Fox, M. D. and Raichle, M. E. (2007) 'Spontaneous fluctuations in brain activity observed with  
849 functional magnetic resonance imaging', *Nat Rev Neurosci*, 8(9), pp. 700-11.
- 850 Fox, M. D., Snyder, A. Z., Vincent, J. L., Corbetta, M., Van Essen, D. C. and Raichle, M. E.  
851 (2005) 'The human brain is intrinsically organized into dynamic, anticorrelated functional  
852 networks', *Proc Natl Acad Sci U S A*, 102(27), pp. 9673-8.
- 853 Friston, K., Moran, R. and Seth, A. K. (2013) 'Analysing connectivity with Granger causality and  
854 dynamic causal modelling', *Curr Opin Neurobiol*, 23(2), pp. 172-8.

- 855 Friston, K. J., Kahan, J., Biswal, B. and Razi, A. (2014) 'A DCM for resting state fMRI',  
856 *Neuroimage*, 94, pp. 396-407.
- 857 Garg, R., Cecchi, G. A. and Rao, A. R. (2011) 'Full-brain auto-regressive modeling (FARM)  
858 using fMRI', *Neuroimage*, 58(2), pp. 416-41.
- 859 Gilson, M., Moreno-Bote, R., Ponce-Alvarez, A., Ritter, P. and Deco, G. (2016) 'Estimation of  
860 Directed Effective Connectivity from fMRI Functional Connectivity Hints at Asymmetries of  
861 Cortical Connectome', *PLoS Comput Biol*, 12(3), pp. e1004762.
- 862 Goebel, R., Roebroeck, A., Kim, D. S. and Formisano, E. (2003) 'Investigating directed cortical  
863 interactions in time-resolved fMRI data using vector autoregressive modeling and Granger  
864 causality mapping', *Magn Reson Imaging*, 21(10), pp. 1251-61.
- 865 Gordon, E. M., Laumann, T. O., Gilmore, A. W., Newbold, D. J., Greene, D. J., Berg, J. J.,  
866 Ortega, M., Hoyt-Drazen, C., Gratton, C., Sun, H., Hampton, J. M., Coalson, R. S., Nguyen, A.  
867 L., McDermott, K. B., Shimony, J. S., Snyder, A. Z., Schlaggar, B. L., Petersen, S. E., Nelson, S.  
868 M. and Dosenbach, N. U. F. (2017) 'Precision Functional Mapping of Individual Human Brains',  
869 *Neuron*, 95(4), pp. 791-807.e7.
- 870 Hacker, C. D., Laumann, T. O., Szrama, N. P., Baldassarre, A., Snyder, A. Z., Leuthardt, E. C.  
871 and Corbetta, M. (2013) 'Resting state network estimation in individual subjects', *Neuroimage*,  
872 82, pp. 616-33.
- 873 Hallquist, M. N., Hwang, K. and Luna, B. (2013) 'The nuisance of nuisance regression: spectral  
874 misspecification in a common approach to resting-state fMRI preprocessing reintroduces noise  
875 and obscures functional connectivity', *Neuroimage*, 82, pp. 208-25.
- 876 He, B. J. (2011) 'Scale-free properties of the functional magnetic resonance imaging signal  
877 during rest and task', *J Neurosci*, 31(39), pp. 13786-95.
- 878 He, B. J., Zempel, J. M., Snyder, A. Z. and Raichle, M. E. (2010) 'The temporal structures and  
879 functional significance of scale-free brain activity', *Neuron*, 66(3), pp. 353-69.
- 880 Hiltunen, T., Kantola, J., Abou Elseoud, A., Lepola, P., Suominen, K., Starck, T., Nikkinen, J.,  
881 Remes, J., Tervonen, O., Palva, S., Kiviniemi, V. and Palva, J. M. (2014) 'Infra-slow EEG  
882 fluctuations are correlated with resting-state network dynamics in fMRI', *J Neurosci*, 34(2), pp.  
883 356-62.
- 884 Hindriks, R., Adhikari, M. H., Murayama, Y., Ganzetti, M., Mantini, D., Logothetis, N. K. and  
885 Deco, G. (2016) 'Can sliding-window correlations reveal dynamic functional connectivity in  
886 resting-state fMRI?', *Neuroimage*, 127, pp. 242-56.
- 887 Hindriks, R., Micheli, C., Bosman, C. A., Oostenveld, R., Lewis, C., Mantini, D., Fries, P. and  
888 Deco, G. (2018) 'Source-reconstruction of the sensorimotor network from resting-state macaque  
889 electrocorticography', *Neuroimage*, 181, pp. 347-358.
- 890 Hlinka, J. and Hadrava, M. (2015) 'On the danger of detecting network states in white noise',  
891 *Front Comput Neurosci*, 9, pp. 11.
- 892 Jenkins, G. M. and Watts, D. G. (1968) *Spectral Analysis and Its Applications*. San Francisco,  
893 CA: Holden-Day.
- 894 Kasdin, N. J. (1995) 'Discrete simulation of colored noise and stochastic processes and  $1/f^a$   
895 power law noise generation', *Proceedings of the IEEE*, 83(5), pp. 802-827.
- 896 Kasdin, N. J. and Walter, T. (1992) 'Discrete simulation of power law noise', *IEEE Freq Control*  
897 *Symp*, pp. 274-283.
- 898 Kendall, M. G. (1954) 'Note on bias in the estimation of autocorrelation', *Biometrika*, 41(3/4), pp.  
899 403-404.
- 900 Laumann, T. O., Gordon, E. M., Adeyemo, B., Snyder, A. Z., Joo, S. J., Chen, M. Y., Gilmore, A.  
901 W., McDermott, K. B., Nelson, S. M., Dosenbach, N. U., Schlaggar, B. L., Mumford, J. A.,  
902 Poldrack, R. A. and Petersen, S. E. (2015) 'Functional System and Areal Organization of a  
903 Highly Sampled Individual Human Brain', *Neuron*, 87(3), pp. 657-70.
- 904 Laumann, T. O., Snyder, A. Z., Mitra, A., Gordon, E. M., Gratton, C., Adeyemo, B., Gilmore, A.  
905 W., Nelson, S. M., Berg, J. J., Greene, D. J., McCarthy, J. E., Tagliazucchi, E., Laufs, H.,

- 906 Schlaggar, B. L., Dosenbach, N. U. and Petersen, S. E. (2016) 'On the Stability of BOLD fMRI  
907 Correlations', *Cereb Cortex*.
- 908 Lin, F. H., Ahveninen, J., Raji, T., Witzel, T., Chu, Y. H., Jääskeläinen, I. P., Tsai, K. W., Kuo,  
909 W. J. and Belliveau, J. W. (2014) 'Increasing fMRI sampling rate improves Granger causality  
910 estimates', *PLoS One*, 9(6), pp. e100319.
- 911 Liu, T. T. (2016) 'Noise contributions to the fMRI signal: An overview', *Neuroimage*, 143, pp.  
912 141-151.
- 913 Liu, X., de Zwart, J. A., Schölvinck, M. L., Chang, C., Ye, F. Q., Leopold, D. A. and Duyn, J. H.  
914 (2018) 'Subcortical evidence for a contribution of arousal to fMRI studies of brain activity', *Nat*  
915 *Commun*, 9(1), pp. 395.
- 916 Liégeois, R., Laumann, T. O., Snyder, A. Z., Zhou, J. and Yeo, B. T. T. (2017) 'Interpreting  
917 temporal fluctuations in resting-state functional connectivity MRI', *Neuroimage*, 163, pp. 437-  
918 455.
- 919 Majeed, W., Magnuson, M., Hasenkamp, W., Schwarb, H., Schumacher, E. H., Barsalou, L. and  
920 Keilholz, S. D. (2011) 'Spatiotemporal dynamics of low frequency BOLD fluctuations in rats and  
921 humans', *Neuroimage*, 54(2), pp. 1140-50.
- 922 Marriott, F. H. C. and Pope, J. A. (1954) 'Bias in the estimation of autocorrelations', *Biometrika*,  
923 41(3/4), pp. 390-402.
- 924 Matsui, T., Murakami, T. and Ohki, K. (2016) 'Transient neuronal coactivations embedded in  
925 globally propagating waves underlie resting-state functional connectivity', *Proc Natl Acad Sci U*  
926 *S A*, 113(23), pp. 6556-61.
- 927 Mitra, A., Kraft, A., Wright, P., Acland, B., Snyder, A. Z., Rosenthal, Z., Czerniewski, L., Bauer,  
928 A., Snyder, L., Culver, J., Lee, J. M. and Raichle, M. E. (2018) 'Spontaneous Infra-slow Brain  
929 Activity Has Unique Spatiotemporal Dynamics and Laminar Structure', *Neuron*, 98(2), pp. 297-  
930 305.e6.
- 931 Mitra, A. and Raichle, M. E. (2016) 'How networks communicate: propagation patterns in  
932 spontaneous brain activity', *Philos Trans R Soc Lond B Biol Sci*, 371(1705).
- 933 Mitra, A. and Raichle, M. E. (2018) 'Principles of cross-network communication in human resting  
934 state fMRI', *Scand J Psychol*, 59(1), pp. 83-90.
- 935 Mitra, A., Snyder, A. Z., Blazey, T. and Raichle, M. E. (2015a) 'Lag threads organize the brain's  
936 intrinsic activity', *Proc Natl Acad Sci U S A*, 112(17), pp. E2235-44.
- 937 Mitra, A., Snyder, A. Z., Constantino, J. N. and Raichle, M. E. (2017) 'The Lag Structure of  
938 Intrinsic Activity is Focally Altered in High Functioning Adults with Autism', *Cereb Cortex*, 27(2),  
939 pp. 1083-1093.
- 940 Mitra, A., Snyder, A. Z., Hacker, C. D., Pahwa, M., Tagliazucchi, E., Laufs, H., Leuthardt, E. C.  
941 and Raichle, M. E. (2016) 'Human cortical-hippocampal dialogue in wake and slow-wave sleep',  
942 *Proc Natl Acad Sci U S A*, 113(44), pp. E6868-E6876.
- 943 Mitra, A., Snyder, A. Z., Hacker, C. D. and Raichle, M. E. (2014) 'Lag structure in resting-state  
944 fMRI', *J Neurophysiol*, 111(11), pp. 2374-91.
- 945 Mitra, A., Snyder, A. Z., Tagliazucchi, E., Laufs, H. and Raichle, M. E. (2015b) 'Propagated  
946 infra-slow intrinsic brain activity reorganizes across wake and slow wave sleep', *Elife*, 4.
- 947 Moddemeijer, R. (1991) 'On the determination of the position of extrema of sampled correlators',  
948 *IEEE T Signal Proces*, 39(1), pp. 216-219.
- 949 Muschelli, J., Nebel, M. B., Caffo, B. S., Barber, A. D., Pekar, J. J. and Mostofsky, S. H. (2014)  
950 'Reduction of motion-related artifacts in resting state fMRI using aCompCor', *Neuroimage*, 96,  
951 pp. 22-35.
- 952 Nikolić, D. (2007) 'Non-parametric detection of temporal order across pairwise measurements of  
953 time delays', *J Comput Neurosci*, 22(1), pp. 5-19.
- 954 Palva, J. M. and Palva, S. (2012) 'Infra-slow fluctuations in electrophysiological recordings,  
955 blood-oxygenation-level-dependent signals, and psychophysical time series', *Neuroimage*,  
956 62(4), pp. 2201-11.

- 957 Pan, W. J., Thompson, G. J., Magnuson, M. E., Jaeger, D. and Keilholz, S. (2013) 'Infraslow  
958 LFP correlates to resting-state fMRI BOLD signals', *Neuroimage*, 74, pp. 288-97.
- 959 Patriat, R., Molloy, E. K. and Birn, R. M. (2015) 'Using Edge Voxel Information to Improve  
960 Motion Regression for rs-fMRI Connectivity Studies', *Brain Connect*, 5(9), pp. 582-95.
- 961 Power, J. D., Barnes, K. A., Snyder, A. Z., Schlaggar, B. L. and Petersen, S. E. (2012) 'Spurious  
962 but systematic correlations in functional connectivity MRI networks arise from subject motion',  
963 *Neuroimage*, 59(3), pp. 2142-54.
- 964 Power, J. D., Cohen, A. L., Nelson, S. M., Wig, G. S., Barnes, K. A., Church, J. A., Vogel, A. C.,  
965 Laumann, T. O., Miezin, F. M., Schlaggar, B. L. and Petersen, S. E. (2011) 'Functional network  
966 organization of the human brain', *Neuron*, 72(4), pp. 665-78.
- 967 Power, J. D., Mitra, A., Laumann, T. O., Snyder, A. Z., Schlaggar, B. L. and Petersen, S. E.  
968 (2014) 'Methods to detect, characterize, and remove motion artifact in resting state fMRI',  
969 *Neuroimage*, 84, pp. 320-41.
- 970 Power, J. D., Plitt, M., Gotts, S. J., Kundu, P., Voon, V., Bandettini, P. A. and Martin, A. (2018)  
971 'Ridding fMRI data of motion-related influences: Removal of signals with distinct spatial and  
972 physical bases in multiecho data', *Proc Natl Acad Sci U S A*, 115(9), pp. E2105-E2114.
- 973 Power, J. D., Plitt, M., Laumann, T. O. and Martin, A. (2017) 'Sources and implications of whole-  
974 brain fMRI signals in humans', *Neuroimage*, 146, pp. 609-625.
- 975 Power, J. D., Schlaggar, B. L. and Petersen, S. E. (2015) 'Recent progress and outstanding  
976 issues in motion correction in resting state fMRI', *Neuroimage*, 105, pp. 536-51.
- 977 Raatikainen, V., Huotari, N., Korhonen, V., Rasila, A., Kananen, J., Raitamaa, L., Keinänen, T.,  
978 Kantola, J., Tervonen, O. and Kiviniemi, V. (2017) 'Combined spatiotemporal ICA (stICA) for  
979 continuous and dynamic lag structure analysis of MREG data', *Neuroimage*, 148, pp. 352-363.
- 980 Satterthwaite, T. D., Ciric, R., Roalf, D. R., Davatzikos, C., Bassett, D. S. and Wolf, D. H. (2017)  
981 'Motion artifact in studies of functional connectivity: Characteristics and mitigation strategies',  
982 *Hum Brain Mapp*.
- 983 Satterthwaite, T. D., Elliott, M. A., Gerraty, R. T., Ruparel, K., Loughead, J., Calkins, M. E.,  
984 Eickhoff, S. B., Hakonarson, H., Gur, R. C., Gur, R. E. and Wolf, D. H. (2013) 'An improved  
985 framework for confound regression and filtering for control of motion artifact in the  
986 preprocessing of resting-state functional connectivity data', *Neuroimage*, 64, pp. 240-56.
- 987 Satterthwaite, T. D., Wolf, D. H., Loughead, J., Ruparel, K., Elliott, M. A., Hakonarson, H., Gur,  
988 R. C. and Gur, R. E. (2012) 'Impact of in-scanner head motion on multiple measures of  
989 functional connectivity: relevance for studies of neurodevelopment in youth', *Neuroimage*, 60(1),  
990 pp. 623-32.
- 991 Scargle, J. D. (1989) 'Studies in astronomical time series analysis. III. Fourier transforms,  
992 autocorrelation functions, and cross-correlation functions of unevenly spaced data', *Astrophys J*,  
993 343, pp. 874-887.
- 994 Schneider, G., Havenith, M. N. and Nikolić, D. (2006) 'Spatiotemporal structure in large neuronal  
995 networks detected from cross-correlation', *Neural Comput*, 18(10), pp. 2387-413.
- 996 Schölvinck, M. L., Maier, A., Ye, F. Q., Duyn, J. H. and Leopold, D. A. (2010) 'Neural basis of  
997 global resting-state fMRI activity', *Proc Natl Acad Sci U S A*, 107(22), pp. 10238-43.
- 998 Siegel, J. S., Mitra, A., Laumann, T. O., Seitzman, B. A., Raichle, M., Corbetta, M. and Snyder,  
999 A. Z. (2017) 'Data Quality Influences Observed Links Between Functional Connectivity and  
1000 Behavior', *Cereb Cortex*, 27(9), pp. 4492-4502.
- 1001 Smith, S. M., Miller, K. L., Salimi-Khorshidi, G., Webster, M., Beckmann, C. F., Nichols, T. E.,  
1002 Ramsey, J. D. and Woolrich, M. W. (2011) 'Network modelling methods for FMRI', *Neuroimage*,  
1003 54(2), pp. 875-91.
- 1004 Snyder, A. Z. and Raichle, M. E. (2012) 'A brief history of the resting state: the Washington  
1005 University perspective', *Neuroimage*, 62(2), pp. 902-10.
- 1006 Stoyanov, M., Gunzburger, M. and Burkardt, J. (2011) 'Pink noise,  $1/f^\alpha$  noise, and their effect on  
1007 solutions of differential equations', *Int J Uncertain Quantification*, 1(3), pp. 257-278.

- 1008 Sun, F. T., Miller, L. M. and D'Esposito, M. (2005) 'Measuring temporal dynamics of functional  
1009 networks using phase spectrum of fMRI data', *Neuroimage*, 28(1), pp. 227-37.
- 1010 Talairach, J. and Tournoux, P. 1988. Co-planar stereotaxic atlas of the human brain. Thieme  
1011 Medical Publishers, New York.
- 1012 Turchi, J., Chang, C., Ye, F. Q., Russ, B. E., Yu, D. K., Cortes, C. R., Monosov, I. E., Duyn, J.  
1013 H. and Leopold, D. A. (2018) 'The Basal Forebrain Regulates Global Resting-State fMRI  
1014 Fluctuations', *Neuron*, 97(4), pp. 940-952.e4.
- 1015 Van Dijk, K. R., Sabuncu, M. R. and Buckner, R. L. (2012) 'The influence of head motion on  
1016 intrinsic functional connectivity MRI', *Neuroimage*, 59(1), pp. 431-8.
- 1017 Walker, W. F. and Trahey, G. E. (1995) 'A fundamental limit on delay estimation using partially  
1018 correlated speckle signals', *IEEE T Ultrason Ferr*, 42(2), pp. 301-308.
- 1019 Wong, C. W., Olafsson, V., Tal, O. and Liu, T. T. (2013) 'The amplitude of the resting-state fMRI  
1020 global signal is related to EEG vigilance measures', *Neuroimage*, 83, pp. 983-90.
- 1021 Yan, C. G., Cheung, B., Kelly, C., Colcombe, S., Craddock, R. C., Di Martino, A., Li, Q., Zuo, X.  
1022 N., Castellanos, F. X. and Milham, M. P. (2013a) 'A comprehensive assessment of regional  
1023 variation in the impact of head micromovements on functional connectomics', *Neuroimage*, 76,  
1024 pp. 183-201.
- 1025 Yan, C. G., Craddock, R. C., He, Y. and Milham, M. P. (2013b) 'Addressing head motion  
1026 dependencies for small-world topologies in functional connectomics', *Front Hum Neurosci*, 7,  
1027 pp. 910.
- 1028 Yeo, B. T., Krienen, F. M., Sepulcre, J., Sabuncu, M. R., Lashkari, D., Hollinshead, M., Roffman,  
1029 J. L., Smoller, J. W., Zöllei, L., Polimeni, J. R., Fischl, B., Liu, H. and Buckner, R. L. (2011) 'The  
1030 organization of the human cerebral cortex estimated by intrinsic functional connectivity', *J*  
1031 *Neurophysiol*, 106(3), pp. 1125-65.
- 1032 Zarahn, E., Aguirre, G. K. and D'Esposito, M. (1997) 'Empirical analyses of BOLD fMRI  
1033 statistics. I. Spatially unsmoothed data collected under null-hypothesis conditions', *Neuroimage*,  
1034 5(3), pp. 179-97.
- 1035
- 1036



1037

1038

1039 **FIGURE LEGENDS**1040 **Figure 1. Computation and visualization of time delays from cross-covariance functions.**

1041 **(A)** Two exemplar ROI time series from the default mode network over  $\sim 200$  s. **(B)** The  
 1042 corresponding CCF (Eq. (5)) is computed here over  $\pm 6.6$  s, which is equivalent to  $\pm 3$  frames as  
 1043 the repetition time was 2.2 s. The time delay (TD;  $\tau_{i,j}$ ) between these time series is the value at  
 1044 which the absolute value of the CCF is maximal. TD can be determined at a resolution finer than  
 1045 the temporal sampling density by parabolic interpolation (red) through the empirical extremum  
 1046 and the points on either side of it (blue) (Eq. (7)). Zero-lag correlation (FC;  $r_{i,j}$ ) is computed from  
 1047 the normalized CCF at zero-lag. **(C)** Toy case illustration of a TD matrix (Eq. (8)) comprising 3  
 1048 voxels. TD matrices contain time delays between every pair of analyzed ROIs and are anti-  
 1049 symmetric by definition. Computing the mean over each column of a TD matrix generates a lag  
 1050 projection map (Eq. (9)), a one-dimensional projection of lag structure **(D)** TD matrix from real  
 1051 rsfMRI data (MSC group average). The rows and columns of this matrix have been sorted from  
 1052 early-to-late and by functional network affiliation. Doing so reveals a range of delays on the  
 1053 order of 1 s both within (on-diagonal) and between (off-diagonal) networks. See text for  
 1054 description of ROIs. **(E)** Example lag projection map computed from the full MSC average TD  
 1055 matrix. The projection identifies regions whose spontaneous activity on average tends to be  
 1056 early (blue) or late (red) with respect to ongoing activity in the rest of the brain (Mitra *et al.*,  
 1057 2014). DAN, dorsal attention network; VAN, ventral attention network; SMN, sensorimotor  
 1058 network; VIS, visual network; FPC, frontoparietal control network; LAN, language network;  
 1059 DMN, default mode network.

1060

1061 **Figure 2. Cross-covariance among discontinuous time series.** **(A)**  $x_1$  and  $x_2$  are two  
 1062 surrogate time series. An example temporal mask shows censored time points in red (zeros).  
 1063 Although  $x_1$  and  $x_2$  share a temporal mask at zero-lag, computing cross-covariance requires that  
 1064 the time series be shifted with respect to one another, and with them, their associated temporal  
 1065 masks. Several shifts of the temporal masks are shown. To compute covariance at a given CCF  
 1066 lag,  $\Delta$ , one could use all pairs of valid frames that align at that lag (all frames in black). This  
 1067 approach maximizes data usage but results in a substantially different number of samples ( $N$ ) at  
 1068 each shift. Alternatively, one could restrict the minimum size of a block of non-censored data at  
 1069 zero-lag such that each block contributes at least one sample to every CCF lag (dark green).  
 1070 The minimum allowable block duration satisfying this requirement, is equal to the total number  
 1071 of lags (i.e.,  $\Delta_{max} + 1 = 4$  frames). This approach would limit (but not eliminate) uneven  
 1072 samples, at the cost of using less data. Note the symmetry of positive and negative CCF lags.  
 1073 Finally, a restriction may be imposed such that an equal number of samples contribute to each  
 1074 CCF lag, although this leads to still further data loss (light green). **(B)** CCFs for two surrogate  
 1075 time series, modeled at  $r = 0.9$  and  $\tau = 1$  s, following censoring with a real temporal mask from  
 1076 a moderate-motion scan (MSC10 session 1). The black and pink CCFs represent the unbiased  
 1077 and biased CCF estimators, respectively. Note the triangular bias in the pink CCF, resulting in a  
 1078  $\hat{\tau}$  value much lower than the true delay. Although the black CCF is quite accurate in this case,  
 1079 the unbiased estimator leads to  $\hat{\tau}$  values that have comparatively higher variance and may often  
 1080 exceed the true delay.

1081

1082 **Figure 3. TDE dependence on data quantity, correlation magnitude, and temporal**  
 1083 **sampling interval.** Surrogate time series ( $\tau = 0.5$  s) reveal strong inverse relationships between  
 1084 TDE accuracy and both **(A)** data quantity (shown for  $r = 0.9$  on a log-log plot spanning several  
 1085 decades) and **(B)** correlation magnitude (shown for 60 minutes of data). Note that longer TRs  
 1086 asymptote at higher RMSE, limiting their precision relative to shorter TRs. **(C)** TDE bias (left)  
 1087 reflects parabolic interpolation bias.  $\hat{\tau}$  values tend to cluster at  $\frac{1}{2}$  multiples of the TR. The  
 1088 variance pattern (right) is attributable to the subsample TDE that is required in fMRI analysis  
 1089 and thus peaks halfway between samples. Combining these two trends yields a pattern in which  
 1090 RMSE increases with increasing temporal distance between  $\tau$  and the nearest TR multiple,  
 1091 save for a trough midway between samples owing to the lack of bias in this region. In all cases,  
 1092 lower TRs yield more favorable results; however, TDE dependence on TR is small relative to  
 1093 data quantity and correlation magnitude. Each data point in the Figure represents a mean  
 1094 across 2,000 simulations.

1095

1096 **Figure 4. Manifestations of sampling error in real rsfMRI data without censoring. (A)**  
 1097 Distributions of pairwise time delays among 264 ROIs (upper triangular of TD matrix) at the  
 1098 session (red), subject (green) and group (black) levels in the MSC dataset. Increasing data  
 1099 quantity reduces sampling error, as indicated by the width of the TD distributions. **(B)**  
 1100 Distributions of all MSC session-level pairwise time delays corresponding to zero-lag correlation  
 1101 magnitudes  $< .2$  (pink) or  $\geq .2$  (blue), as determined by the MSC average correlation matrix. The  
 1102 increased width of the pink distribution results from sampling error associated with weaker  
 1103 correlations. The wide distribution also makes the bias of parabolic interpolation readily  
 1104 observable: time delay estimates cluster around the TR (here, 2.2 s) and slope discontinuities  
 1105 appear at every  $\frac{1}{2}$  TR.

1106

1107 **Figure 5. Temporal structure in intra- and inter-network relationships is obscured by**  
 1108 **sampling error. (A)** Subject-level (MSC01) TD (left) and  $|FC|$  (right) matrices comprising 6 mm  
 1109 gray matter cube ROIs grouped by functional network (as in Fig. 1D). **(B)** Toy case illustrating  
 1110 computation of blockwise diagonal “error” (non-square blocks are first interpolated to yield  
 1111 square blocks). TD matrix blocks in (A) that appear more organized seem to comprise (roughly)  
 1112 iso-latent diagonals. Thus, temporal structure of a given block (submatrix) can be estimated as  
 1113 the RMSE of all time delays in the block relative to the mean delay of their respective diagonals.  
 1114 Error of the perfectly structured toy submatrix amounts to 0. Repeating this process for each  
 1115 unique block yields an error matrix. **(C)** Toy case illustrating computation of the mean  $|FC|$   
 1116 matrix. **(D)** MSC01 error and mean  $|FC|$  matrices computed from the TD and  $|FC|$  matrices  
 1117 shown in (A). Submatrices were interpolated to be square before computing diagonals. (The  
 1118 main diagonal is all zeroes by definition and therefore excluded in error computations). **(E)** Error  
 1119 in temporal structure as a function of mean  $|FC|$ , computed for the 28 unique network blocks at  
 1120 the session (MSC01 session 1), subject (MSC01) and group (MSC average) levels. Error is  
 1121 strongly inversely correlated with FC magnitude at the session and subject levels. At the group  
 1122 level (3,000 minutes of data), this correlation is not significant. Note overall decrease in error  
 1123 and leftward shift of  $|\hat{\tau}|$  values associated with increasing data. (\*\*\*\* $p < .0001$ ;  $N = 28$  blocks).  
 1124 DAN, dorsal attention network; VAN, ventral attention network; SMN, sensorimotor network;  
 1125 VIS, visual network; FPC, frontoparietal control network; LAN, language network; DMN, default  
 1126 mode network.

1127

1128 **Figure 6. Sampling error arising from aggressive data exclusion. (A)** Scatter plots  
 1129 illustrating the relationship between TD distribution width, as measured by the standard  
 1130 deviation ( $\sigma_{TD}$ ), and head motion/data loss, as measured by mean FD. Each point represents  
 1131 one MSC session, color-coded by subject. Pre-censoring plots reflect a relationship with head  
 1132 motion, while post-censoring plots predominantly reflect sampling error. Censoring exacerbates  
 1133 an already positive relationship between mean FD and  $\sigma_{TD}$ . **(B)** Same as in (A), but for FC.  
 1134 Following censoring, the relationship between  $\sigma_{FC}$  and mean FD changes from significantly  
 1135 negative to significantly positive. **(C)** Distribution of correlations between  $|TD|$  and mean FD,  
 1136 across all 100 sessions. Each data point included in the QC:|TD| histogram corresponds to a  
 1137 single ROI pair. Null distributions, computed by randomly permuting mean FD values, are  
 1138 centered near zero (black). Higher motion sessions show modestly greater magnitude time  
 1139 delays (left) before censoring (red); this effect is exacerbated after data exclusion (blue) due to  
 1140 increased sampling error in higher-motion sessions. **(D)** Same as in (C), but for  $|FC|$ . Censoring  
 1141 leads to inflated  $|FC|$  (blue). **(E)** The left panel shows intra-subject correspondence (Spearman's  
 1142 rho) of the vectorized TD matrix averaged across the five lowest- and highest-motion sessions  
 1143 for each subject. The right panel shows, for each subject, mean correspondence between each  
 1144 session's TD matrix and the censored group average. Error bars denote standard deviation. **(F)**  
 1145 Same as in (E), but for FC, and correspondence is measured as Pearson's  $r$ . In both (D) and  
 1146 (E), stringent motion criteria adversely impact reliability ( $*p < .05$ ;  $**p < .01$ ;  $***p < .001$ ;  $N = 10$   
 1147 for Low:High motion correspondence,  $N = 100$  for Group correspondence).

1148

1149 **Figure 7. Including small blocks of clean data improves intra- and inter-subject reliability**  
 1150 **of TD and FC. (A)** Same plots as in Figure 6E-F, but for different minimum imposed block  
 1151 durations. The minimum allowable block duration (min) is 8.8 s ( $(\Delta_{max} + 1) \times TR$ ). **(B)** Same as  
 1152 in (A), but for FC.

1153

1154 **Figure 8. Censoring-induced sampling error in TD, but not FC, remains observable with**  
 1155 **minimum allowable block duration. (A)** Post-censoring  $\sigma$ :FD scatter plots as in the right  
 1156 panels of Figure 6A-B, but for minimum imposed block duration equivalent to the minimum  
 1157 allowable (rather than 60 seconds, as in Fig. 6). **(B)** Same distributions as in Figure 6C-D, but  
 1158 only post-censoring and for minimum allowable block duration. Censoring-induced sampling  
 1159 error inflates  $|TD|$  even with minimum allowable block duration, but this is less apparent for FC.

1160

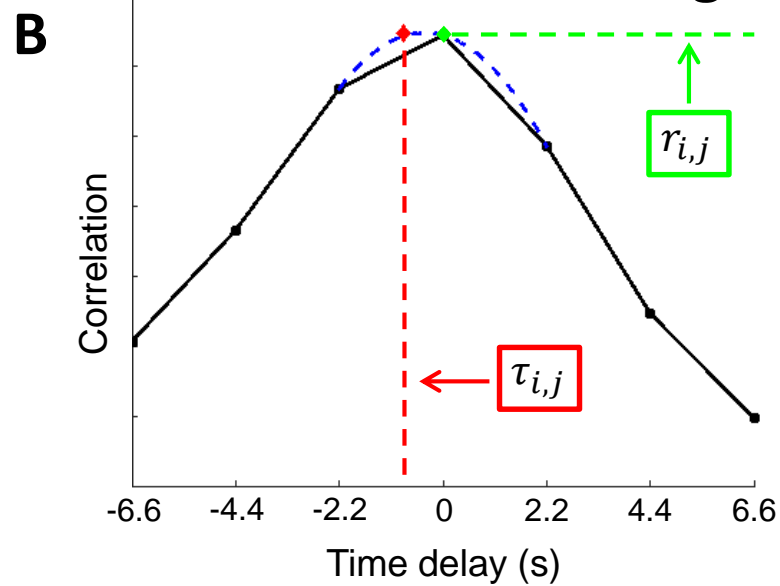
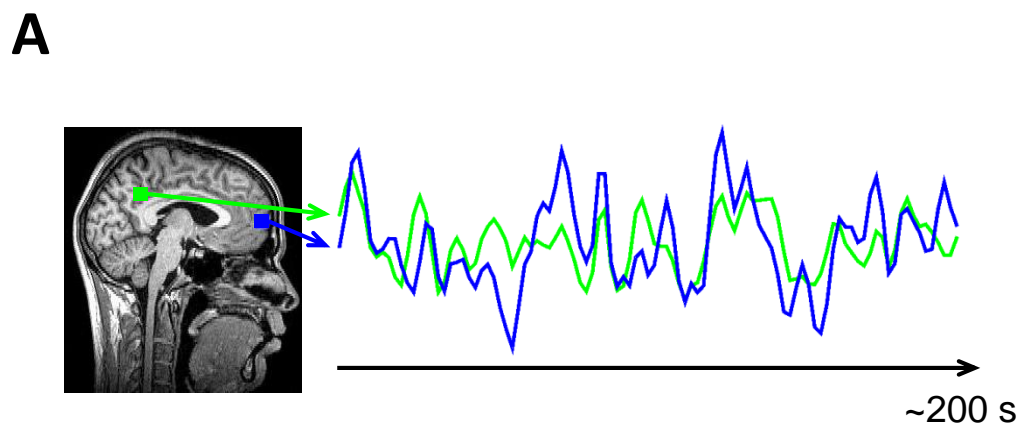
1161 **Figure 9. Censoring-induced sampling error in TD and FC computed from surrogate data**  
 1162 **remains substantial with minimum allowable block duration. (A)** Post-censoring  $\sigma$ :FD  
 1163 scatter plots as in Figure 8A, but for TD and FC distributions computed from surrogate data. The  
 1164 100 real, session-specific temporal censoring masks were applied to a single set of surrogate  
 1165 time series, which was constructed from the MSC average 264 x 264 FC matrix (no lags were  
 1166 built in). Note that the group average correlation distribution is narrower than that obtained from  
 1167 single sessions; thus  $\sigma_{TD}$  values are somewhat larger than in Figure 8A (more sampling error)  
 1168 and  $\sigma_{FC}$  values are generally smaller than in Figure 8A. **(B)** Same distributions as in Figure 8B,  
 1169 but for TD and FC computed from surrogated data as described above. Effects of censoring-  
 1170 induced sampling error are still present with minimum allowable block duration.

1171

1172 **Figure 10.  $|FC|$ -weighted lag projections improve reliability. (A)** Modeling the relationship  
 1173 between TDE error and zero-lag correlation magnitude. By adjusting a single parameter,  $\beta$ , Eq.

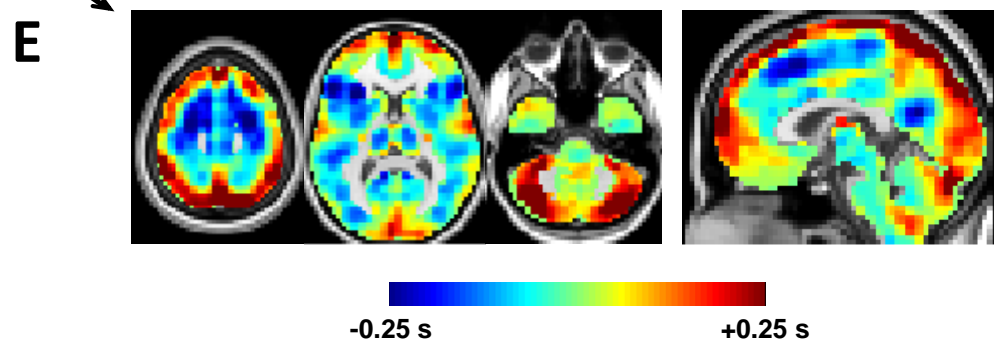
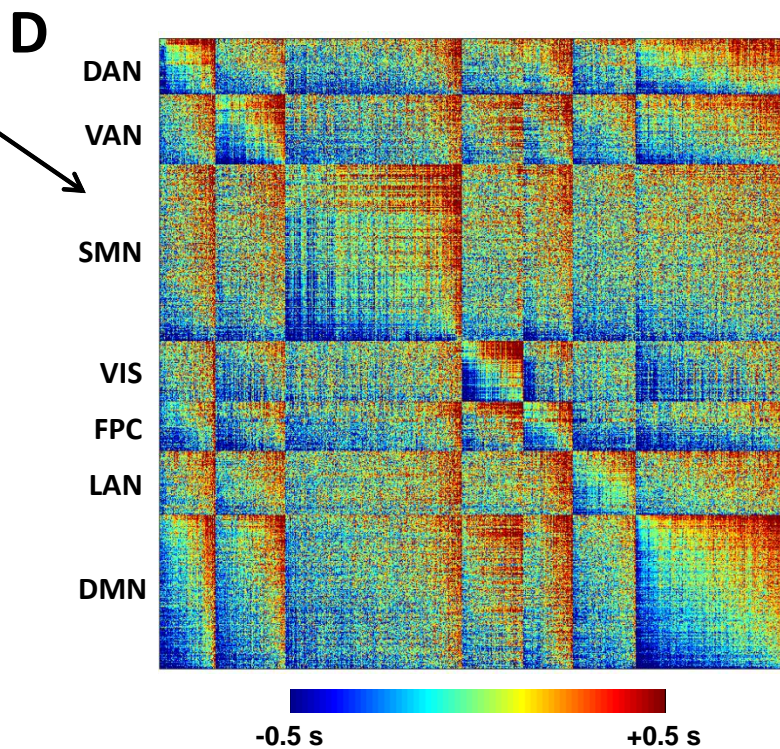
1174 (15) (red) captures this relationship well for a range of data quantities and TRs. For each data  
1175 quantity,  $\beta$  and  $R^2$  values are based on fit to 2 s TR. **(B)** Example unweighted (top) and  
1176 weighted (bottom) lag projections for MSC01 session 1 (left), MSC01 (middle; TD averaged  
1177 over all 10 sessions prior to lag projection computation), and MSC01-10 (right; TD first averaged  
1178 over all 100 sessions). **(C)**  $\sigma$ :FD plots depicting the width of the distributions of lag projection  
1179 values for each MSC session as a function of mean FD. Weighting increases distribution widths  
1180 as well as the relationship between distribution width and data loss. **(D)** Correspondence of  
1181 session-level unweighted and weighted lag projections with group *unweighted* lag projection.  
1182 Weighting strongly improves reliability. (\*\* $p < .001$ ).

**Fig. 1**

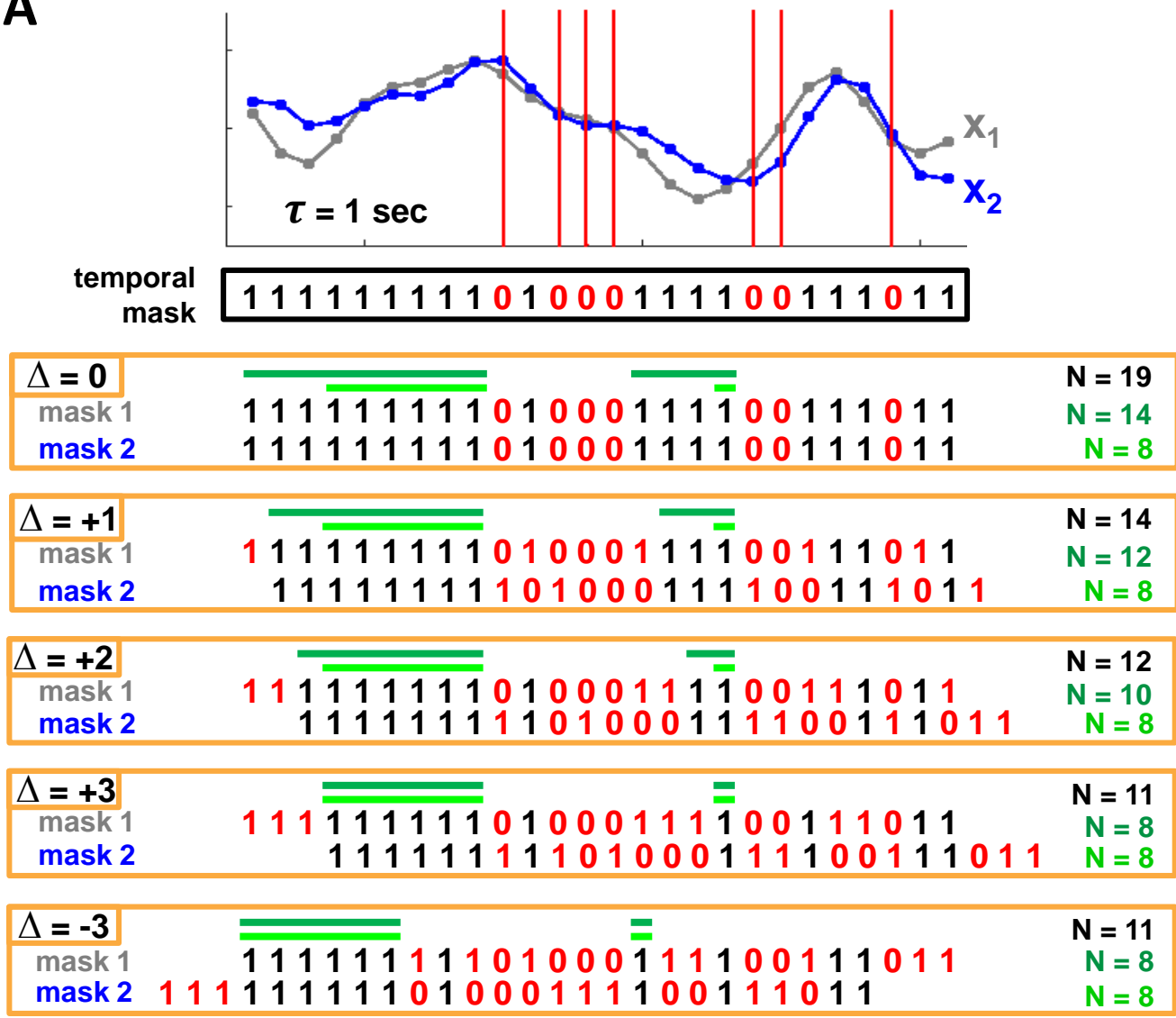


**C**

ROI	1	2	3
1	0	$\tau_{1,2}$	$\tau_{1,3}$
2	$-\tau_{1,2}$	0	$\tau_{2,3}$
3	$-\tau_{i,3}$	$-\tau_{2,3}$	0
Mean	$-\frac{1}{3}(\tau_{1,2} + \tau_{1,3})$	$\frac{1}{3}(\tau_{1,2} - \tau_{2,3})$	$\frac{1}{3}(\tau_{1,3} + \tau_{2,3})$



A



B

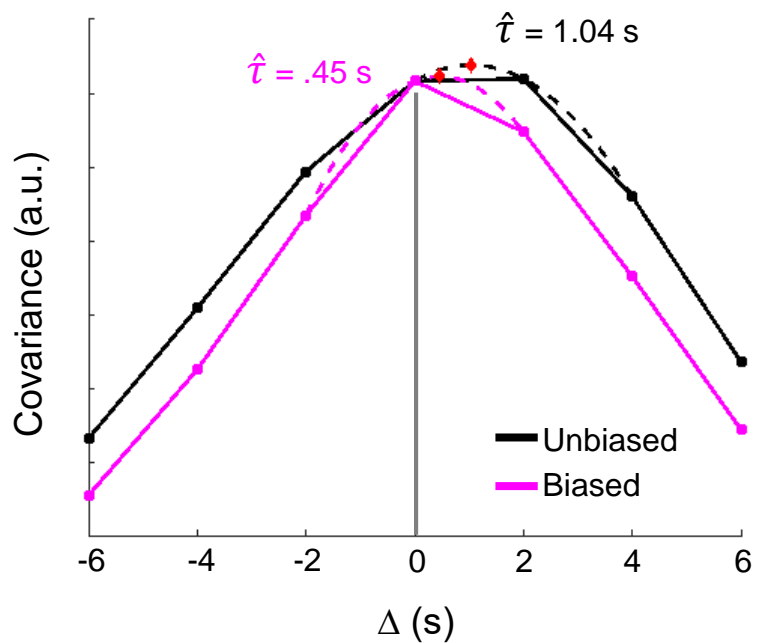


Fig. 3

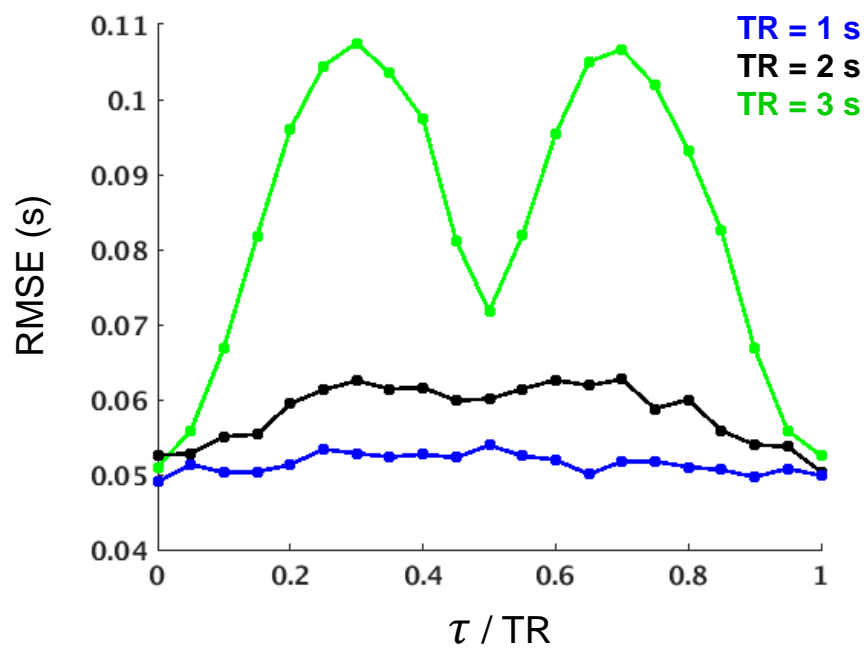
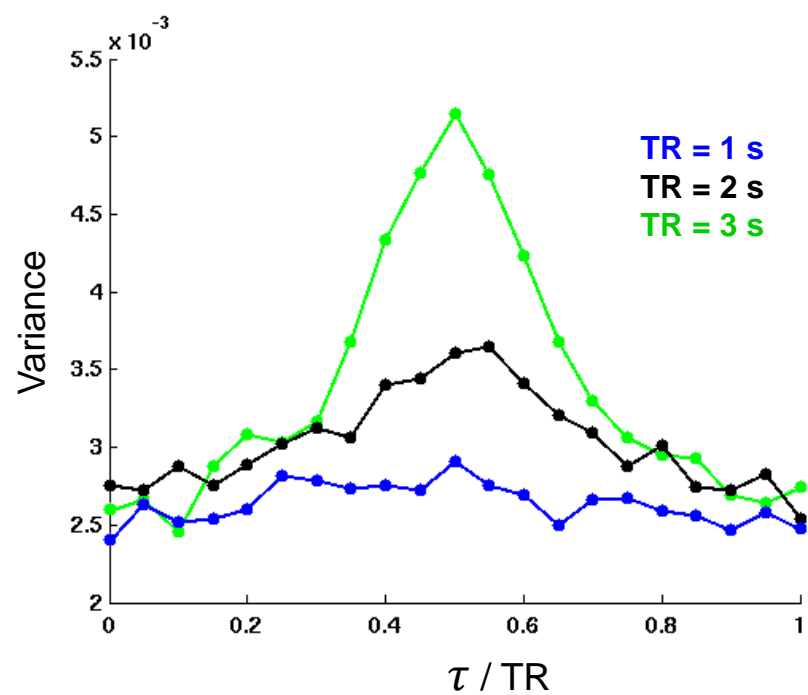
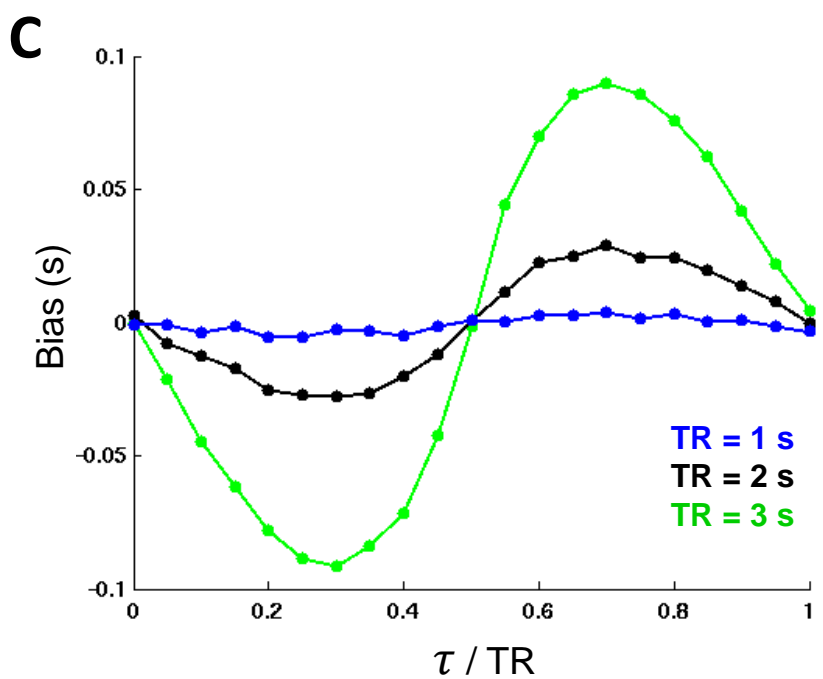
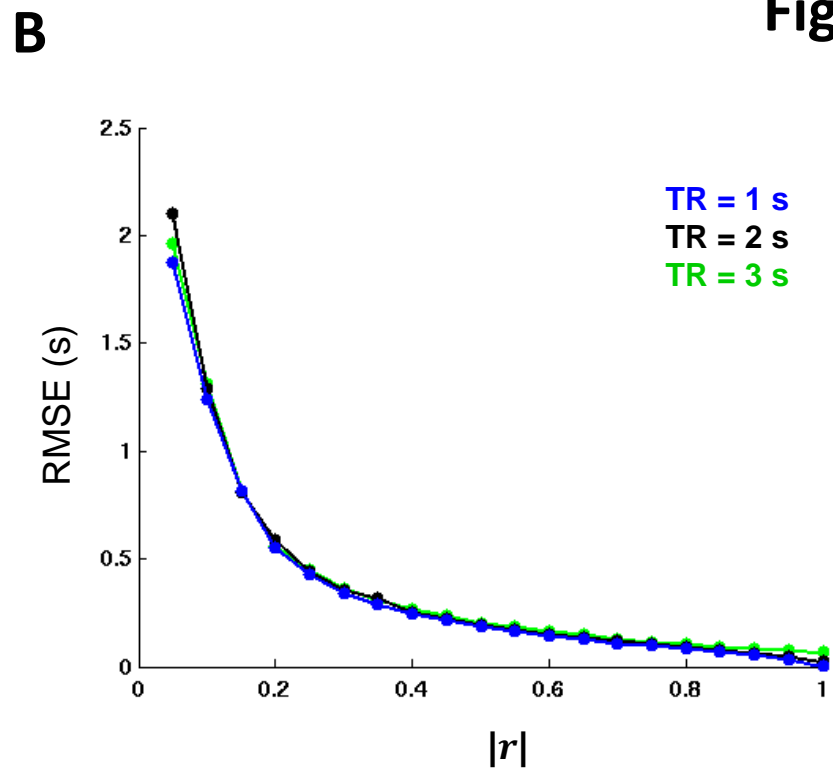
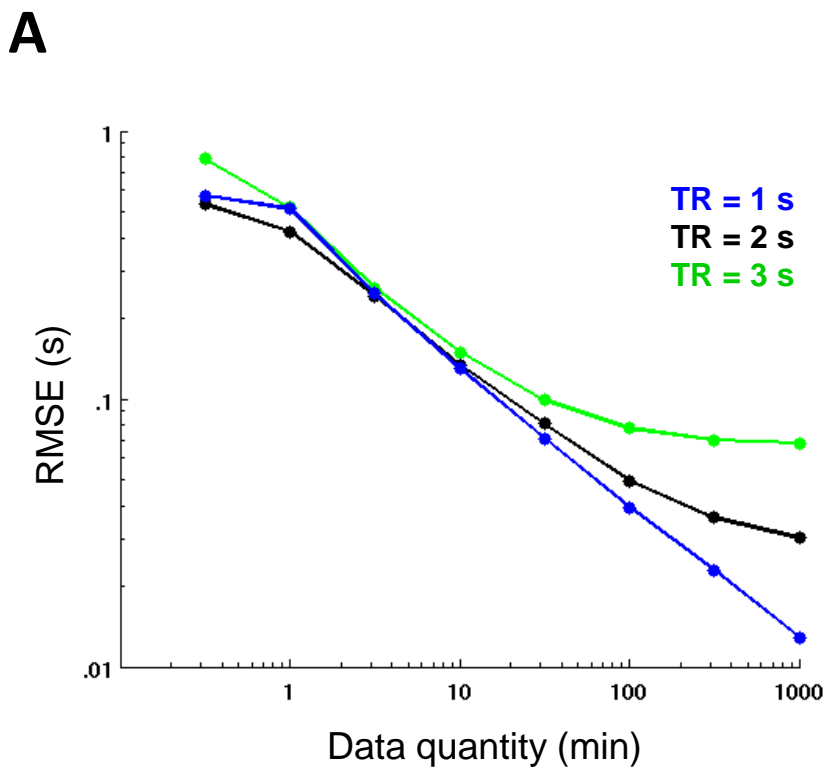
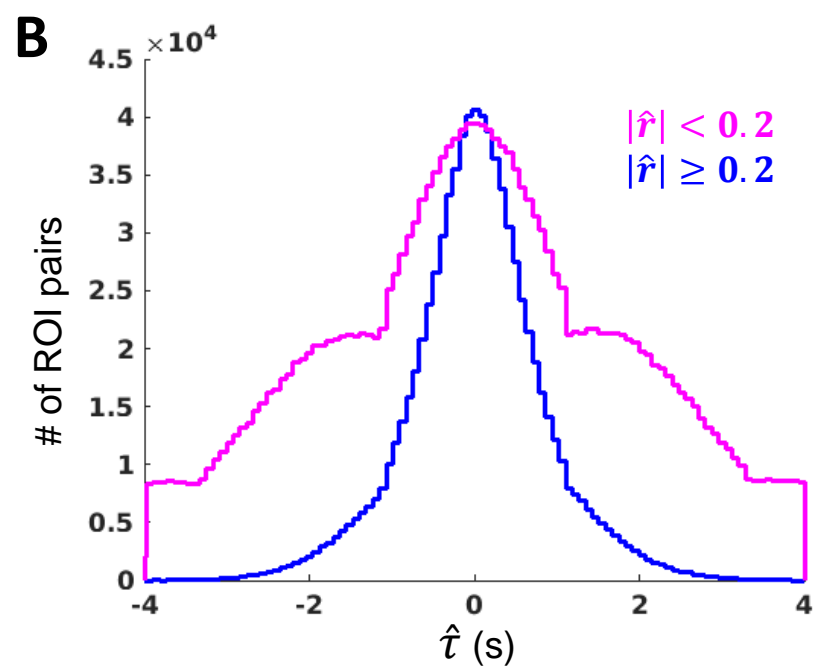
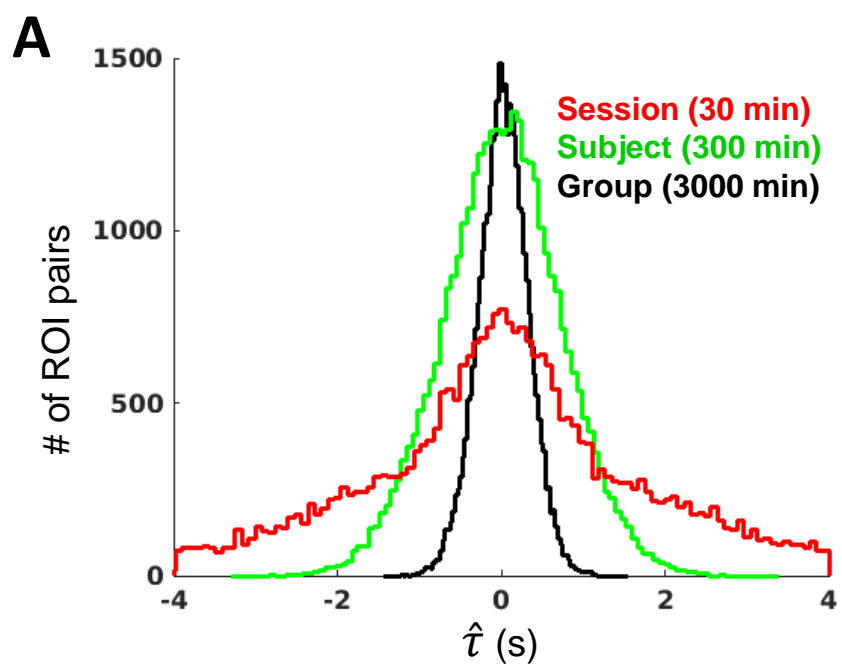
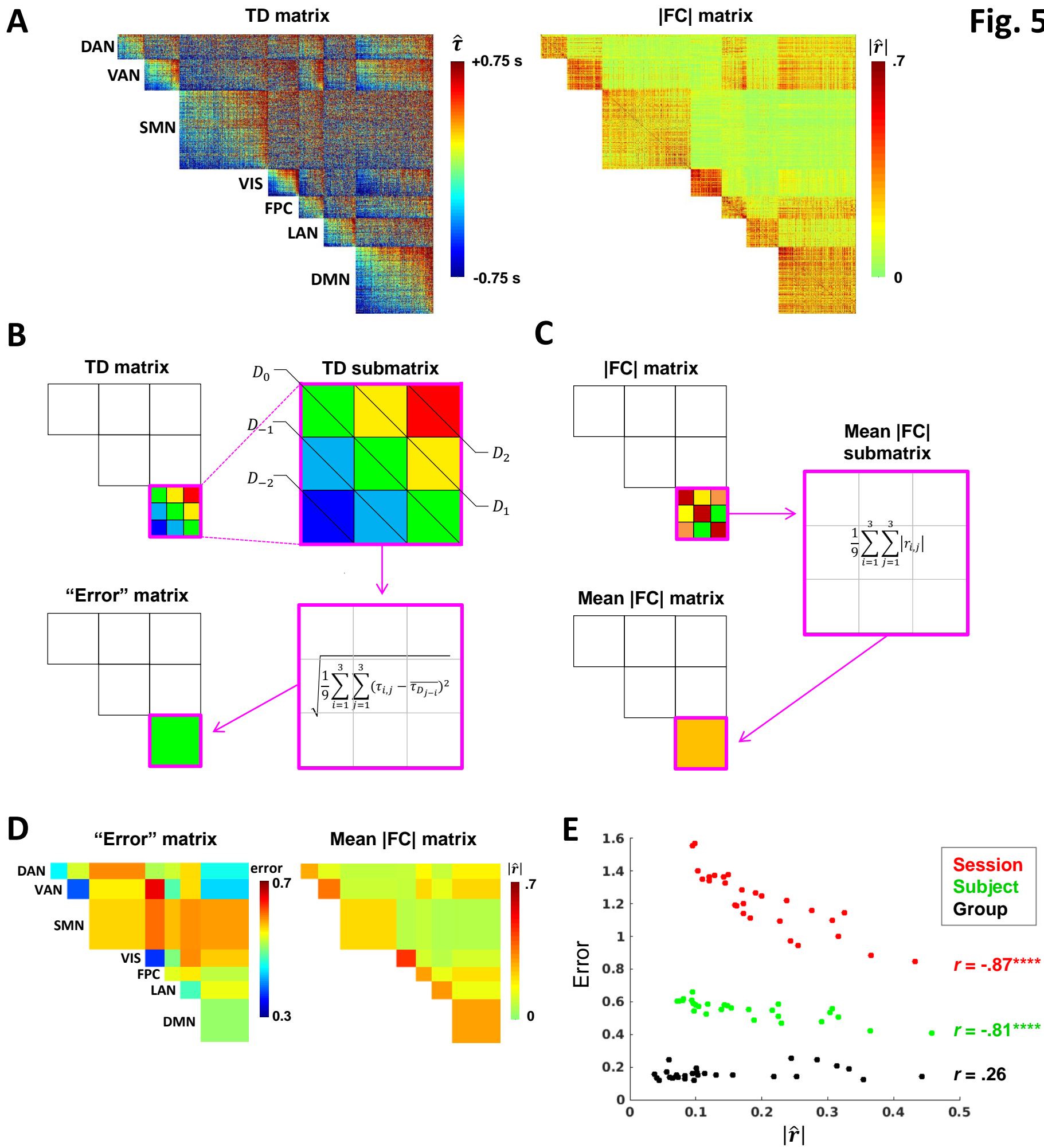


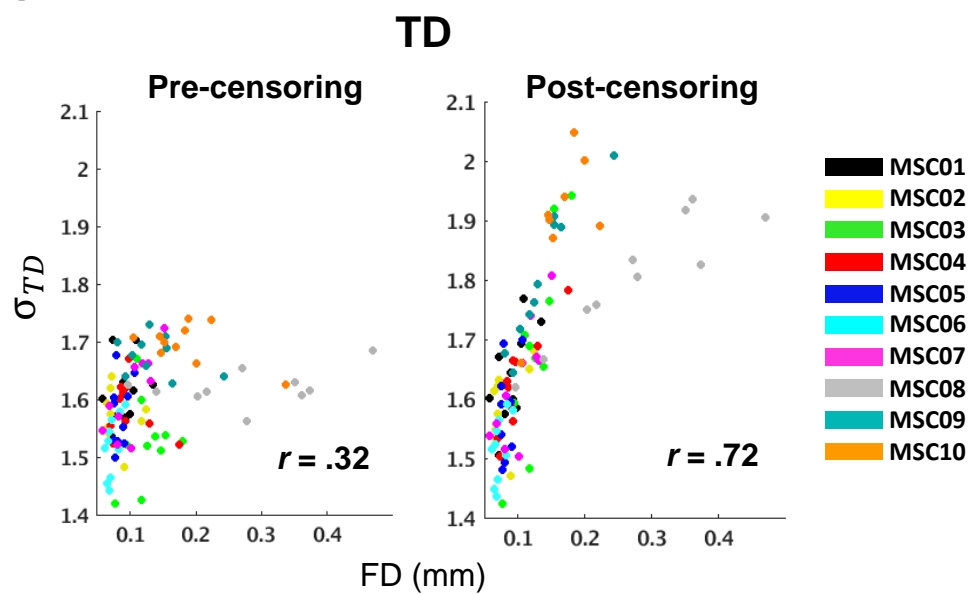
Fig. 4



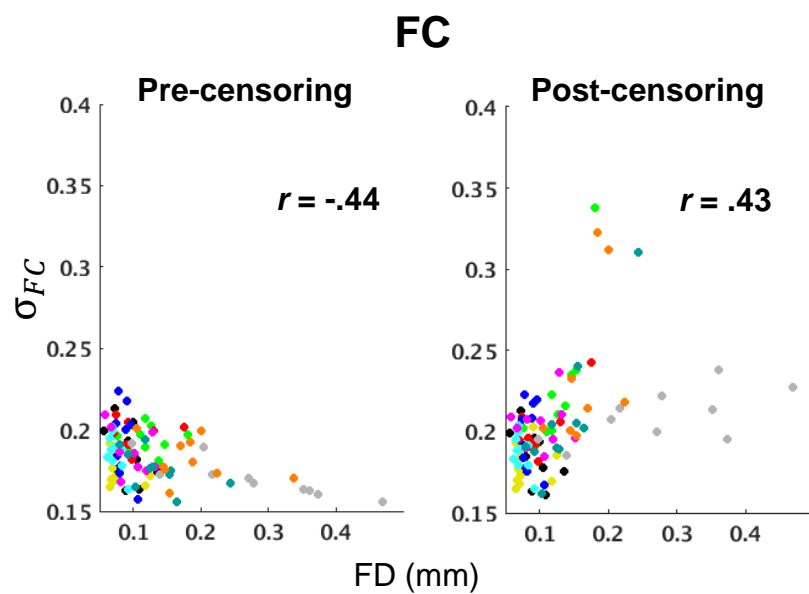




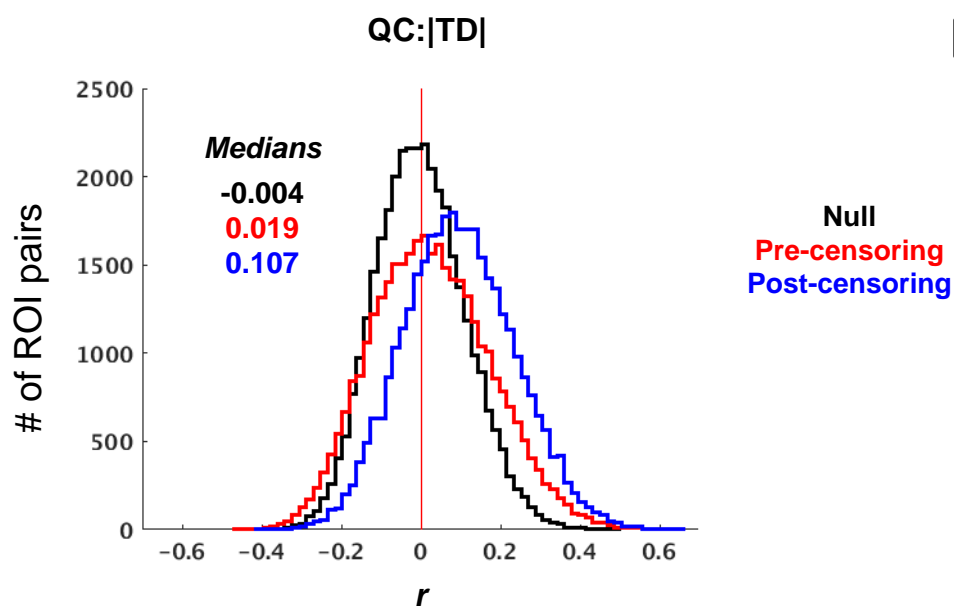
A



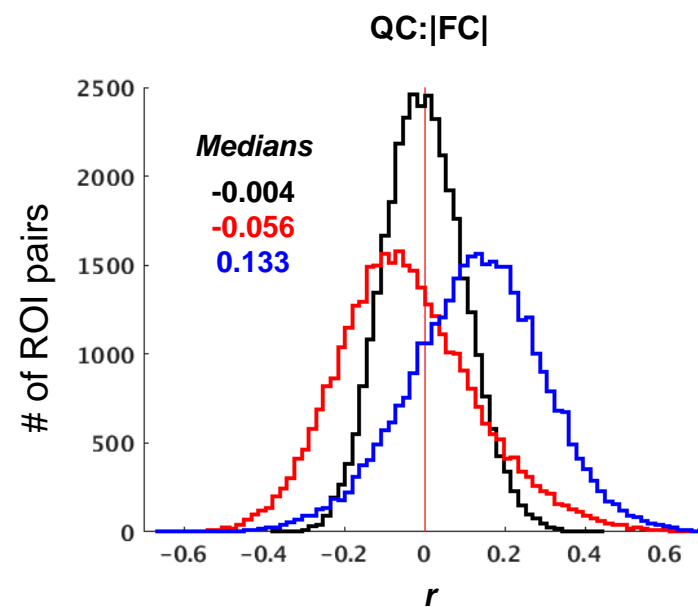
B



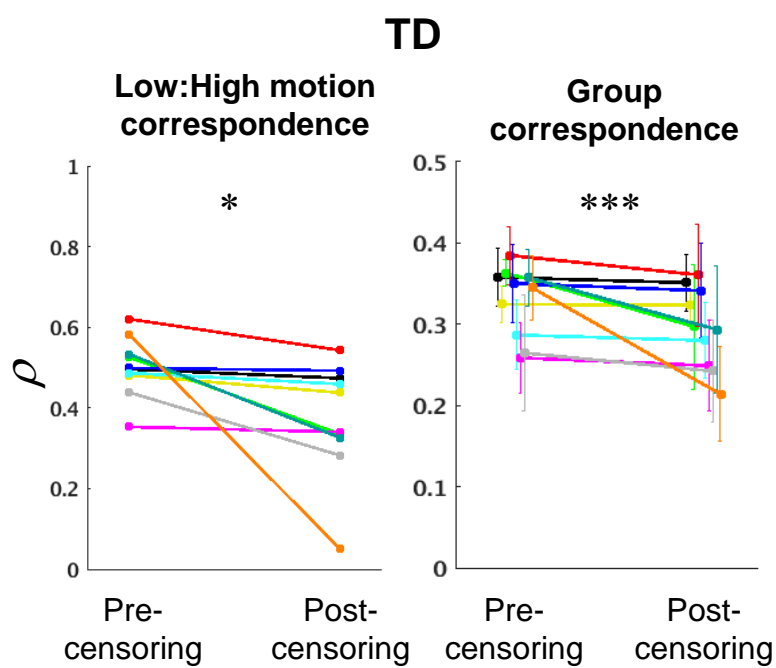
C



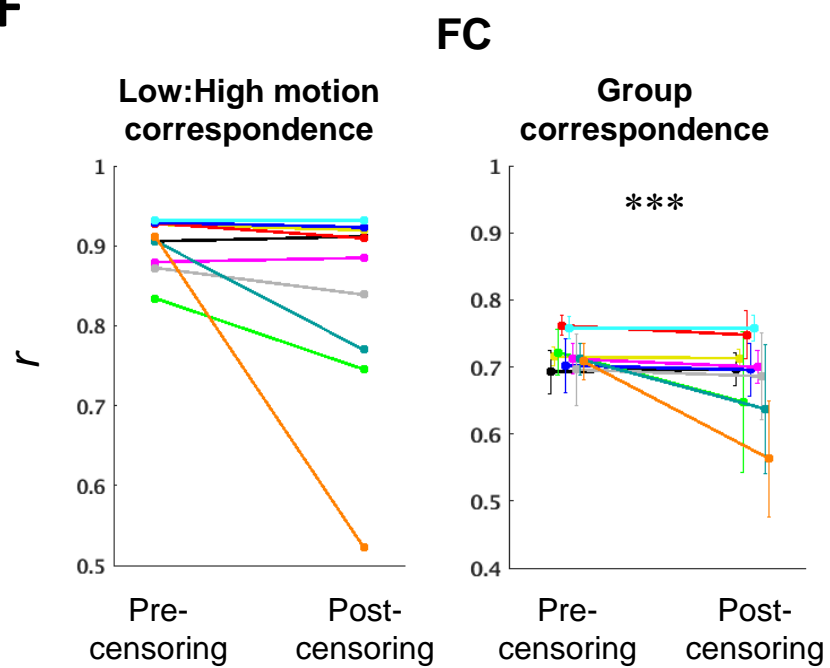
D



E

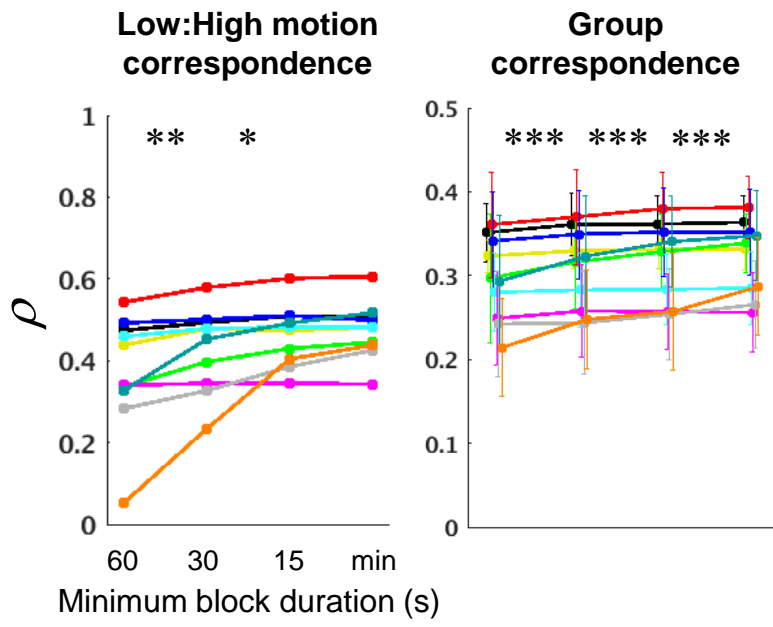


F



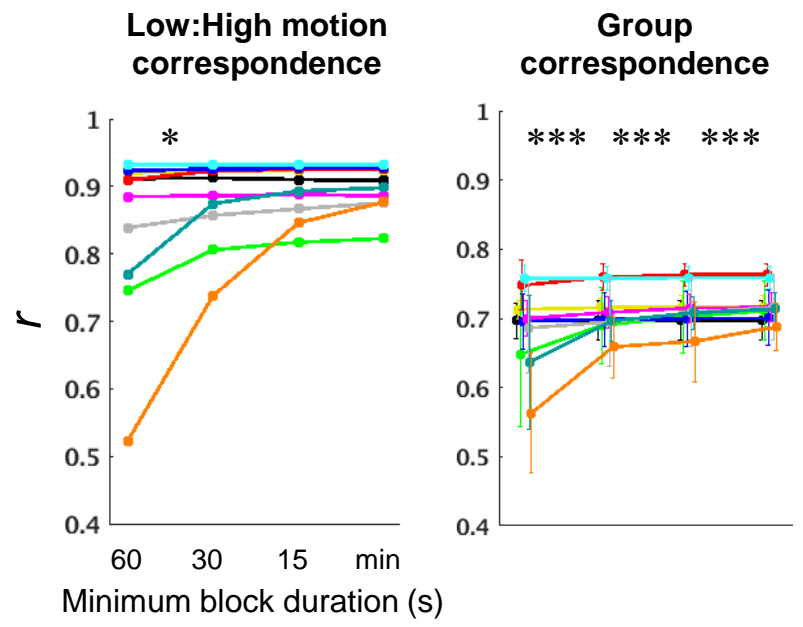
A

TD

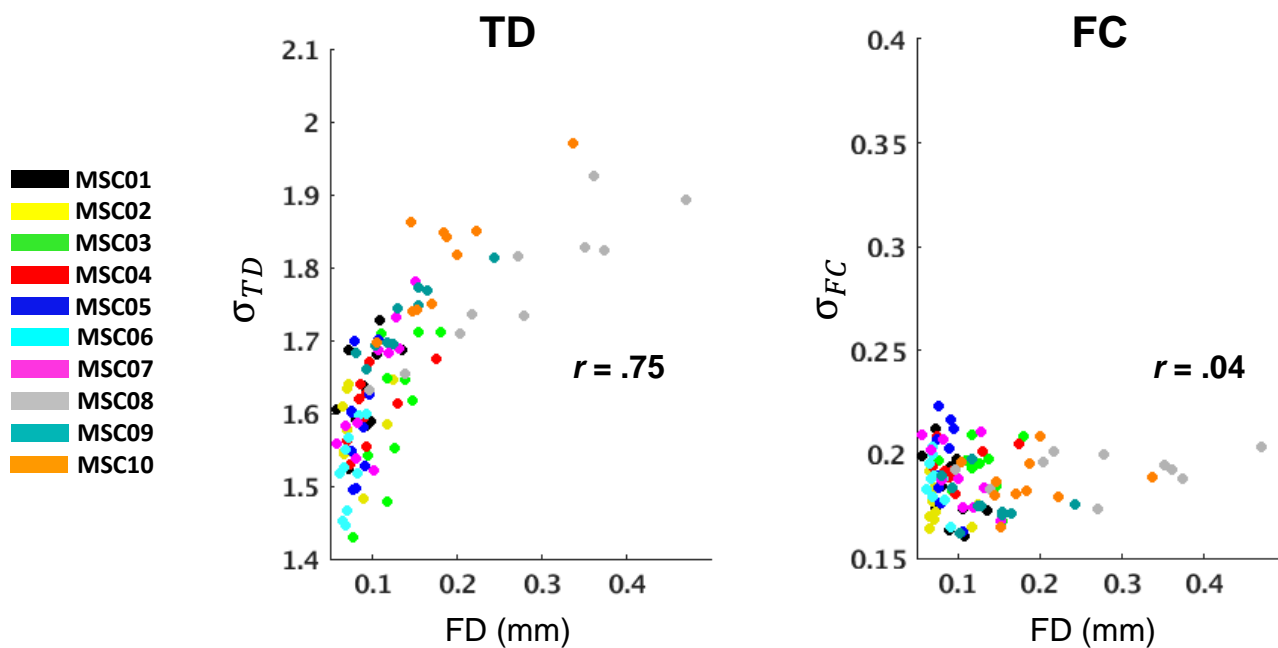


B

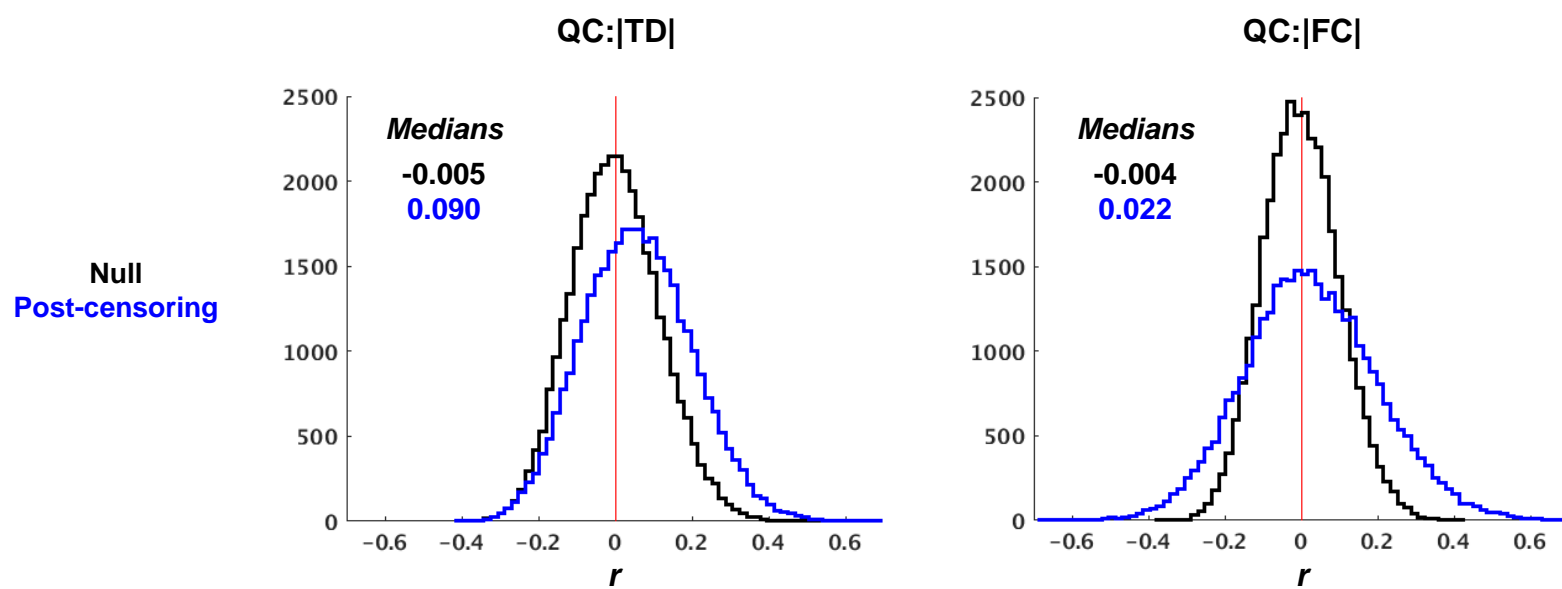
FC



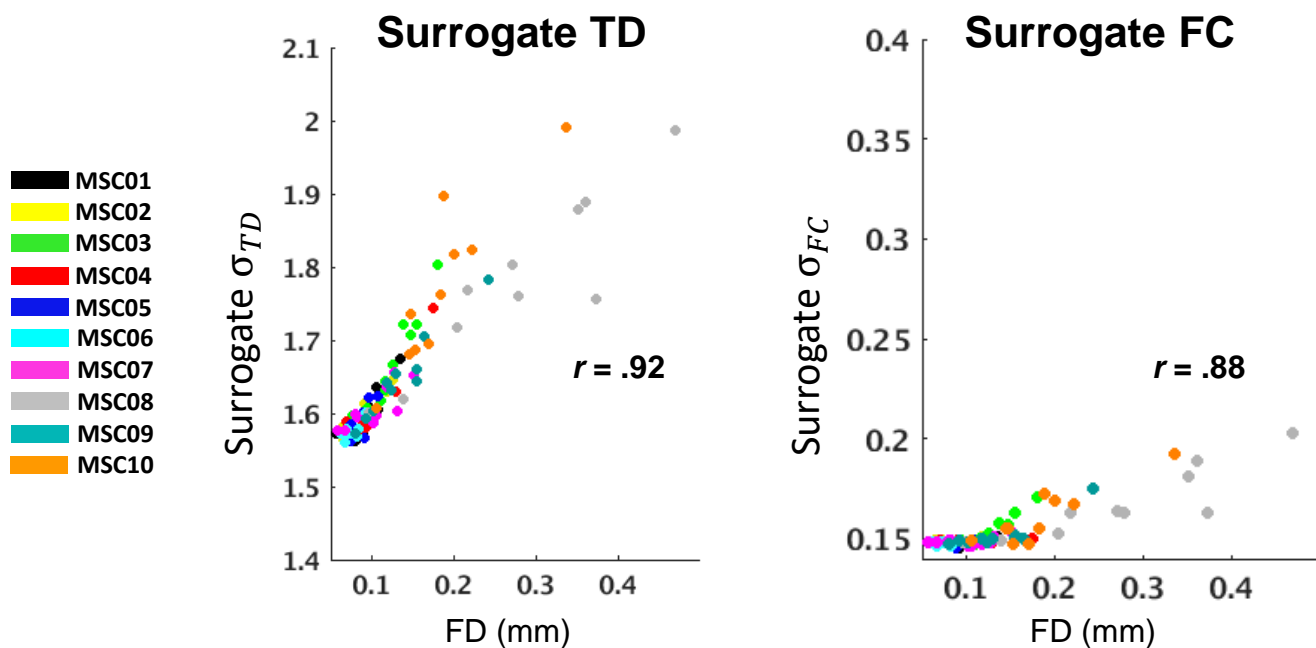
A



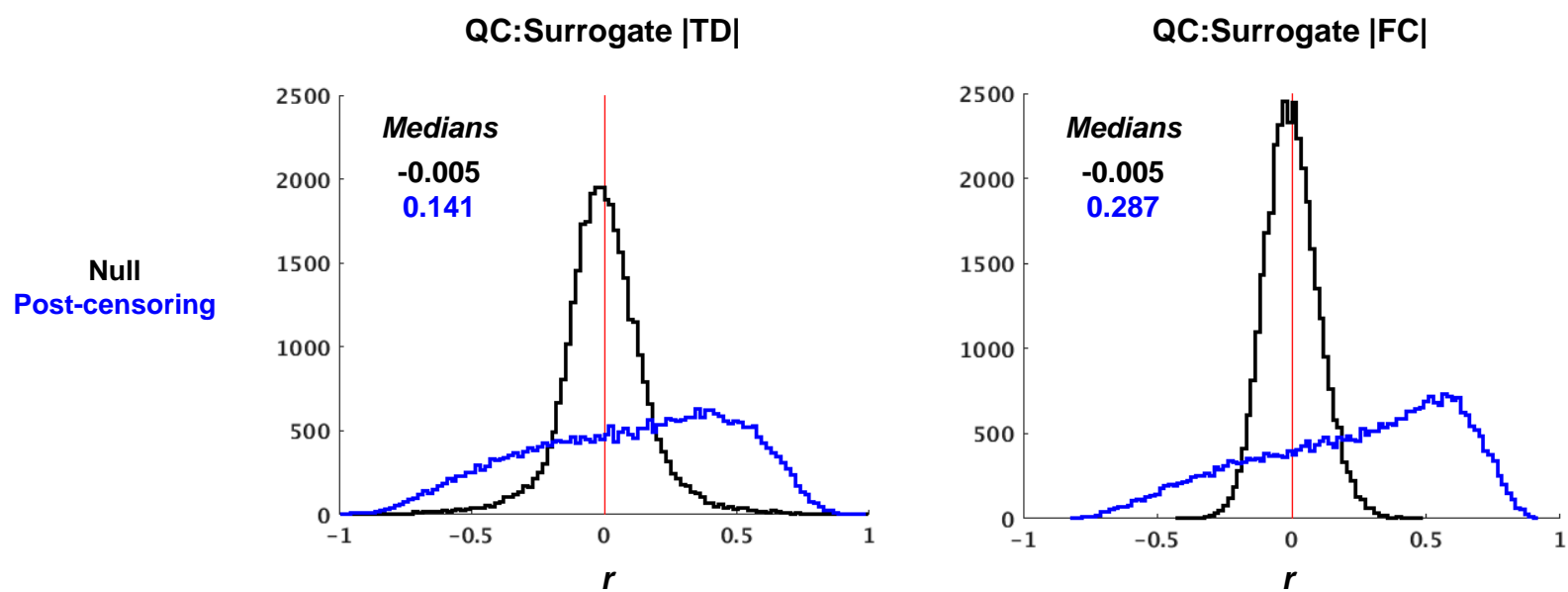
B

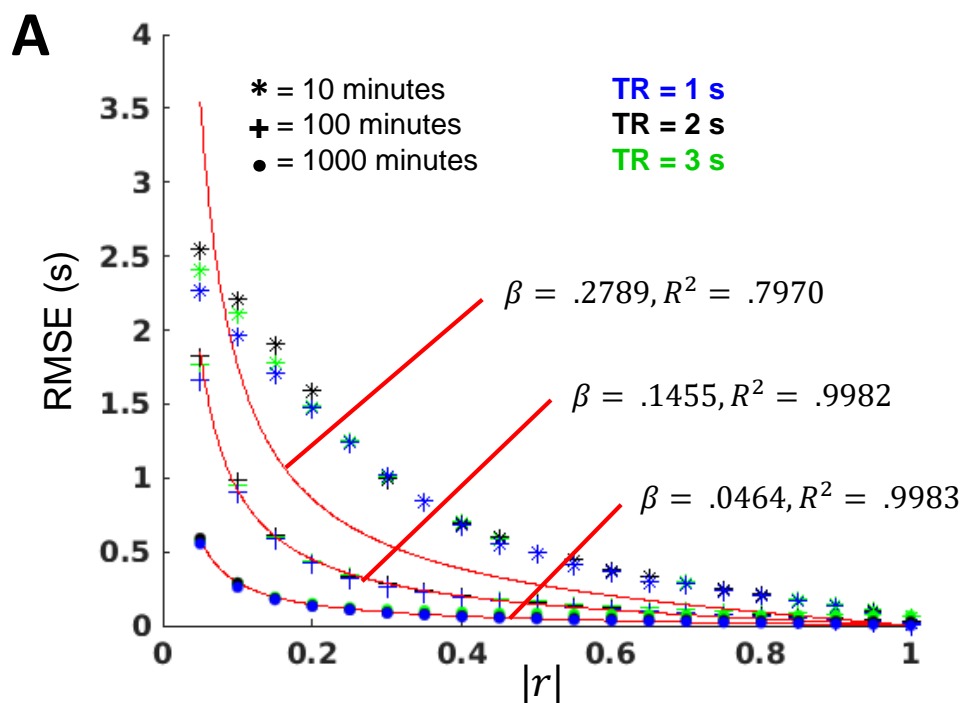


A

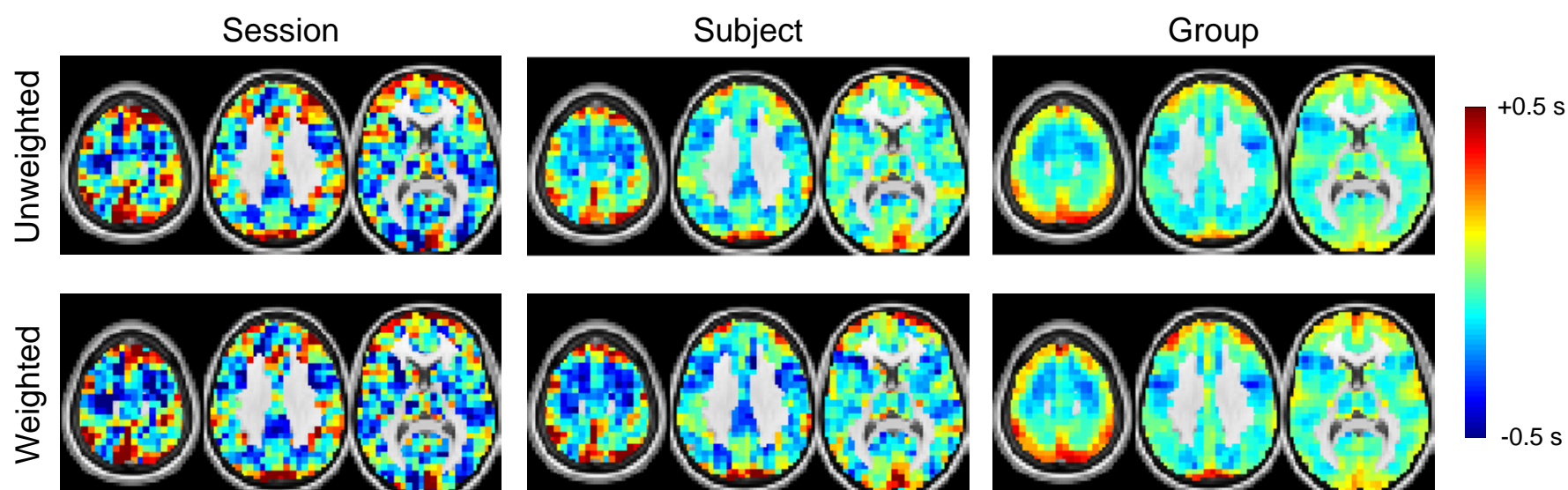


B

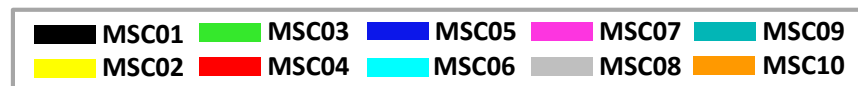
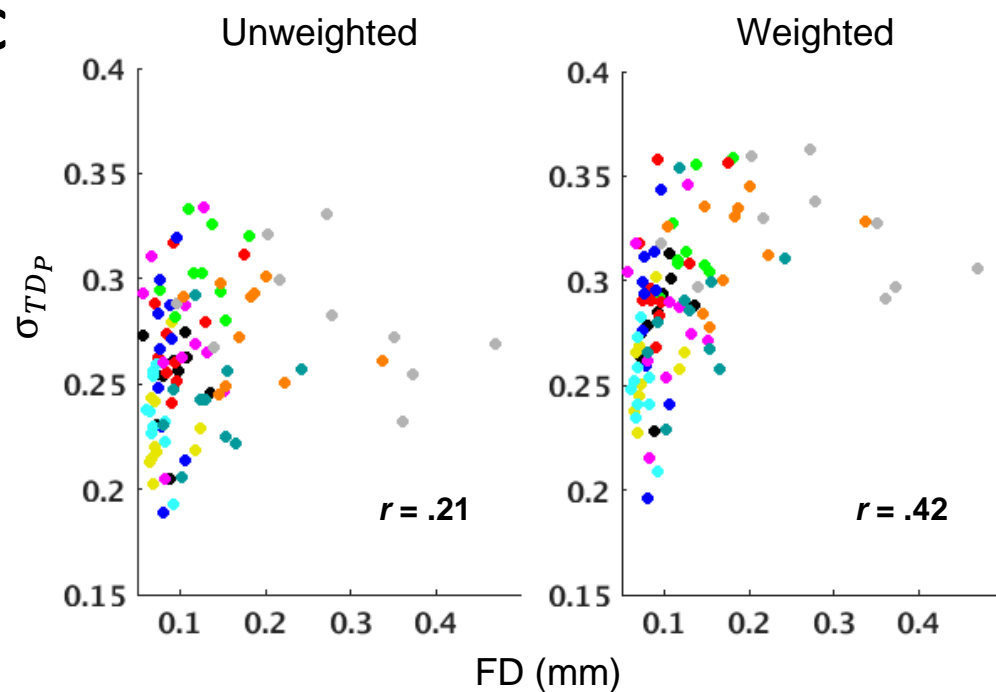




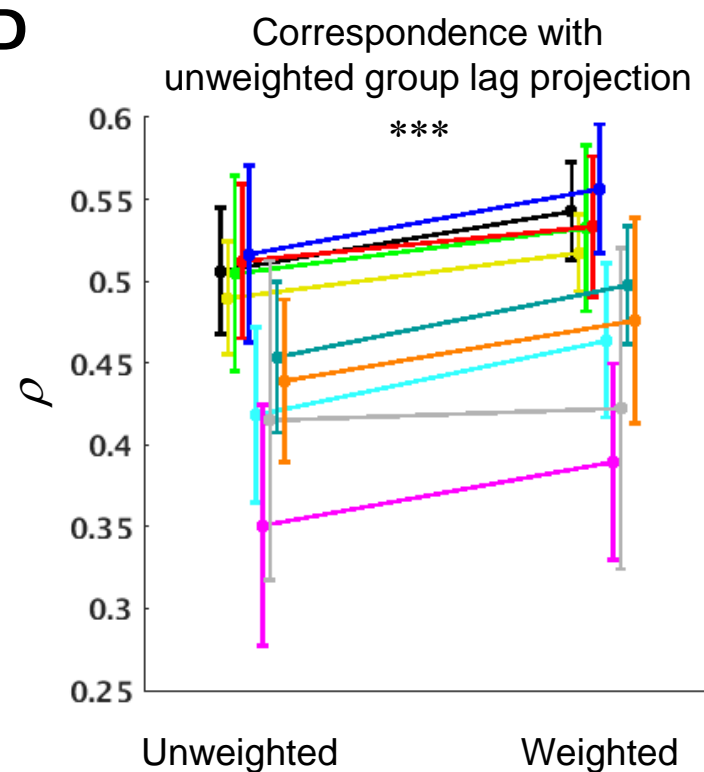
**B**



**C**



**D**



Supplementary figures